

# Galactic fountains and outflows in star forming dwarf galaxies: ISM expulsion and chemical enrichment

C. Melioli,<sup>1,2\*</sup> F. Brighenti<sup>3</sup> and A.D’Ercole<sup>1</sup>

<sup>1</sup>*INAF-Osservatorio Astronomico di Bologna, via Ranzani 1, 40126 Bologna, Italy*

<sup>2</sup>*IAG - Universidade de São Paulo, Rua do Matão 1226, São Paulo, Brazil*

<sup>3</sup>*Dipartimento di Fisica e Astronomia, Università di Bologna, via Ranzani 1, 40126 Bologna, Italy*

Accepted ... Received ...; in original form ...

## ABSTRACT

We investigated the impact of supernova feedback in gas-rich dwarf galaxies experiencing a low-to-moderate star formation rate, typical of relatively quiescent phases between starbursts. We calculated the long term evolution of the ISM and the metal-rich SN ejecta using 3D hydrodynamic simulations, in which the feedback energy is deposited by SNeII exploding in distinct OB associations. We found that a circulation flow similar to galactic fountains is generally established, with some ISM lifted at heights of one to few kpc above the galactic plane. This gas forms an extra-planar layer, which falls back to the plane in  $\approx 10^8$  yr, once the star formation stops. Very little or no ISM is expelled outside the galaxy system for the considered SFRs, even though in the most powerful model the SN energy is comparable to the gas binding energy. The metal-rich SN ejecta is instead more vulnerable to the feedback and we found that a significant fraction (25 – 80%) is vented in the intergalactic medium, even for low SN rate ( $7 \times 10^{-5} - 7 \times 10^{-4} \text{ yr}^{-1}$ ). About half of the metals retained by the galaxy are located far ( $z > 500$  pc) from the galactic plane. Moreover, our models indicate that the circulation of the metal-rich gas out from and back to the galactic disk is not able to erase the chemical gradients imprinted by the (centrally concentrated) SN explosions.

## Key words:

galaxies: dwarf – galaxies: ISM – galaxies: intergalactic medium – ISM: kinematics and dynamics – ISM: abundances – ISM: evolution

## 1 INTRODUCTION

Dwarf galaxies evolution is likely affected by both external and internal processes such as tidal and ram pressure stripping, and galactic winds (see Tolstoy et al. 2009, for a detailed review). In particular, the interplay between Type II supernova (hereafter indicated simply as SN) explosions, stellar winds and interstellar medium (ISM) has important effects on the formation and the dynamical and chemical evolution of these systems. Main characteristics of a dwarf galaxy are low metallicities, low surface brightness and low mass. Given their shallow potential, these galaxies can in principle lose a significant fraction of their ISM during the burst of SN explosions (e.g. Dekel & Silk 1986; De Young & Heckman 1994; Mac Low & Ferrara 1999; D’Ercole & Brighenti 1999), and this could lead to a cessation of star formation and to the

inability to retain newly synthesized metals (external processes as ram pressure and tidal stripping are also expected to play a role; see, e.g., Mayer et al. 2006; Marcolini et al. 2006). The SN feedback may be the key to understand the possible link between the evolution of dwarf irregular galaxies (dIrrs) to dwarf spheroidal galaxies (dSphs), as pointed out by many authors (see, e.g., Loose & Thuan 1986; Dekel & Silk 1986; Silk et al. 1987; Davies & Phillipps 1988). However, while it is plausible that the star formation feedback has a crucial impact in the life of dwarf galaxies, the complexity of the interaction between the supernovae and the ISM still prevents a detailed comprehension of this process.

The effect of the star formation heating must depend, among other things, on the star formation rate (SFR), the ISM density and spatial distribution and the depth of the galactic potential well. A large fraction of (irregular and blue compact) dwarf galaxies host star formation (SF) episodes, and clustered SNe are responsible for the formation of superbubbles, outflows or galactic winds. However, without a

\* E-mail: cmelioli@astro.iag.usp.br; fabrizio.brighenti@unibo.it; annibale.dercole@oabo.inaf.it

direct measurement of the gas dynamics, it is difficult to understand whether the outflowing gas can escape the gravitational potential of the dwarf galaxy or it remains bound to the system to fall back at later times (cf. Creasey et al. 2013, and references therein).

Recently, a number of high resolution numerical models of feedback from supernovae have been worked out to study in detail the role of the magnetic field (Hill et al. 2012) or to obtain physically motivated sub-grid description of winds that can be implemented in cosmological hydrodynamic simulations and phenomenological models (Creasey et al. 2013). These authors, as others before (Korpi et al. 1999; de Avillez 2000; de Avillez & Berry 2001; de Avillez & Breitschwerdt 2004, 2005a,b) simulate only a small volume of galactic disk in order to obtain high spatial resolutions. SPH simulations with pc-scale resolutions taking into account the whole galaxy have been presented by Hopkins et al. (2012).

In this paper we study the large scale and long term evolution of the gas ejected by SN explosions in a typical dwarf galaxy. Our aim is to study the relation between SFR, mass loss and metallicity gradient evolution. Abundance gradients in dwarf galaxies are observed to be essentially flat (e.g. Lagos et al. 2009; Werk et al. 2011; Lagos et al. 2012, and references therein), leading to the conclusion that one or more physical processes exist able to distribute metals throughout the gas disk. Metal mixing may be favoured by SN driven winds carrying metals which can fall back down at large radii, by gas disk turbulence and by past interactions which have led to the accretion of external gas. In this work we test the impact of gas flows (wind, outflow, fountains) on the metal abundance evolution.

Outflows and galactic winds were studied by many authors both analytically (see, e.g., Shapiro & Field 1976; Bregman 1980) and numerically by hydrodynamical simulations (e.g. Tomisaka & Ikeuchi 1986; D’Ercole & Brighenti 1999; Mac Low & Ferrara 1999; Strickland & Stevens 2000; Recchi et al. 2001; Mori et al. 2002; Recchi et al. 2002; Fragile et al. 2004; Hopkins et al. 2012; Recchi & Hensler 2013; Melioli et al. 2013). In these works it is investigated how the development and evolution of galactic winds depend on the gravitational potential, total gas and stellar mass, ISM density and temperature, SFR.

Melioli et al. (2008, 2009) considered the occurrence of galactic fountains in Milky Way-like galaxies. They showed that the majority of the gas lifted up in our Galaxy by the Galactic fountains falls back on the disk remaining quite close to the place where the fountains originated, thus not influencing the radial chemical gradients on large scale. However, in the case of dwarf galaxies, it is plausible that the smaller size and the shallower potential allow for a more effective redistribution of metals incorporated in galactic flows.

To test such a possibility, we run 3D numerical simulations of star formation feedback in a galaxy of total mass of  $\sim 10^{10} M_{\odot}$ , taking into account different SFRs and different durations of the SN explosions. The numerical grid used here includes the whole rotating galaxy, and the adaptive mesh scheme allows us to follow in detail the ejected gas, while the remaining galactic volume is mapped at a lower resolution.

In the following sections, we describe the numerical pro-

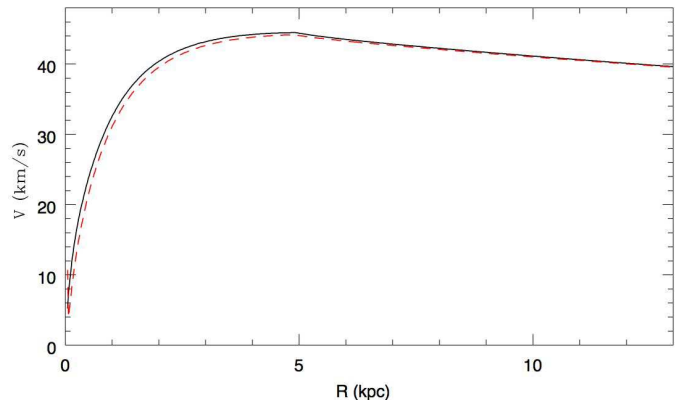


**Figure 1.** Circular velocity profile (solid line) and ISM rotational velocity profile in the  $z = 0$  plane.

cedure (Section 2). The basic results of the simulations are outlined in Section 3, while in Section 4 we discuss in detail the evolution of each model. Finally, in Section 5 we draw our conclusions.

## 2 THE MODELS

### 2.1 The dwarf galaxy

In this Section we describe the dwarf galaxy model. We set the initial conditions for the ISM following the procedure outlined in Melioli et al. (2008). In brief, we first assume a mass model for the galaxy, which includes the contribution of a stellar disk and of a spherical dark matter halo. Then, we build the ISM in rotational equilibrium in the galactic potential, by specifying the 3D density distribution and computing the temperature and azimuthal velocity distributions.

The gravitational potential of the stellar disk is assumed to be generated by a density distribution following a flattened King profile

$$\rho_{\star}(r) = \frac{\rho_{\star,0}}{\left[1 + (R/R_{\star,c})^2 + (z/z_{\star,c})^2\right]^{3/2}}. \quad (1)$$

where  $\rho_{\star,0}$  is the central density of the stars, and  $R_{\star,c}$  and  $z_{\star,c}$  are the core radii. In this model we take  $\rho_{\star,0} = 2 \times 10^{-24} \text{ g cm}^{-3}$ ,  $R_{\star,c} = 1.2 \text{ kpc}$  and  $z_{\star,c} = 0.67 \text{ kpc}$ . The stellar distribution is assumed to extend up to  $R_{\star,t} = 4.8 \text{ kpc}$  and  $z_{\star,t} = 2.6 \text{ kpc}$ . The gravitational potential  $\Phi_{\star}$  associated to this stellar disk is computed numerically following the method described in Brighenti & Mathews (1996).

Finally, the gravitational potential of the dark matter halo is assumed to follow the Navarro, Frenk and White profile (Navarro et al. 1996)

$$\Phi_{\text{dm}}(r) = -\frac{GM_{\text{vir}}}{r_s f(c)} \frac{\ln(1+x)}{x}, \quad (2)$$

where  $M_{\text{vir}}$  is the mass at the virial radius  $r_{\text{vir}}$  (defined as the radius where the average density is  $102\rho_{\text{crit}}$ , being  $\rho_{\text{crit}}$  the cosmic critical density),  $x = r/r_s$ ,  $r$  is the spherical radius,  $r_s$  is a scale radius,  $c = r_{\text{vir}}/r_s$  is the concentration, and  $f(c) = \ln(1+c) - c/(1+c)$ . In this model we have  $M_{\text{vir}} = 10^{10} M_{\odot}$ ,  $r_{\text{vir}} = 55.3 \text{ kpc}$ ,  $r_s = 2.94 \text{ kpc}$  and  $c = 18.8$ , adopting

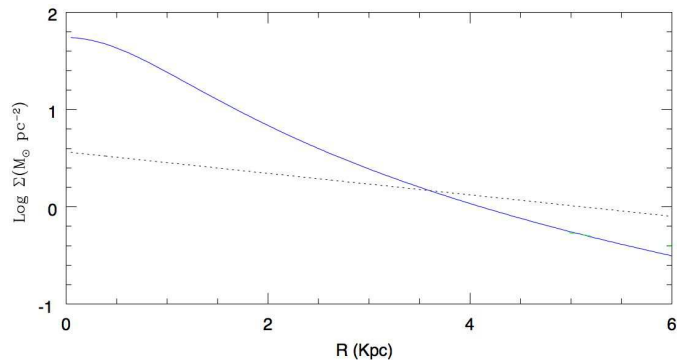


**Figure 2.** Stellar (solid line) and gas (dotted line) mass surface density for the dwarf galaxy model (face-on). Distances are given in kpc and densities are in  $M_{\odot}/\text{pc}^2$ . The values refer only to the “upper half galaxy” ( $z > 0$ ) covered by the computational grid. The values for the whole galaxy are just twice as those indicated.

a  $\Lambda$  cold dark matter cosmological universe with  $\Omega_M=0.27$ ,  $\Omega_{\Lambda}=0.73$  and  $H_0=71 \text{ km s}^{-1} \text{ Mpc}^{-1}$ . The resulting circular velocity as a function of radius (in the  $z = 0$  plane) is shown in Figure 1 (solid line).

The assumed 3D gas density distribution writes:

$$\rho = \frac{\Sigma_d}{2z_d} \exp\left(-\frac{R}{R_d} - \frac{|z|}{z_d}\right), \quad (3)$$

where  $R$  is the cylindrical radius,  $z$  is the vertical height,  $R_d$  and  $z_d$  are respectively the radial and the vertical scale height of the disk, and  $\Sigma_d$  is a characteristic surface density. In this study we assume  $R_d = 4 \text{ kpc}$ ,  $z_d = 170 \text{ pc}$  and  $\Sigma_d = 8 M_{\odot} \text{ pc}^{-2}$ . The total gas mass within the computational box (see below) is  $M_g \sim 1.5 \times 10^8 M_{\odot}$ . While these parameters are not designed to describe any specific galaxy, they are generally consistent with observed irregular dwarf galaxies, and, in particular, with the low surface brightness dwarf galaxies studied by van Zee et al. (1997). The stellar and gas surface densities are shown in Figure 2, while the values of the galactic parameters are summarized in Table 1.

In order to set the gas in a configuration of rotating equilibrium in the total potential well described above, the pressure at any point is found by integrating the  $z$ -component of the hydrostatic equilibrium equation for any value of the disk radius  $R$ . The integration starts at the outermost values of  $z$  (where we can assume the pressure  $P = 0$ ) and proceeds inward to reach the galactic plane at  $z = 0$ . This procedure defines the pressure (and hence the temperature) in the whole space. Unperturbed initial pressure, temperature and density distributions for this model are shown in Figure 3.

The azimuthal velocity  $v_{\phi}(R, z)$  of the gas is found by balancing in the  $R$ -direction the accelerations due to the centrifugal and gravitational forces as well as to the pressure gradient (Figure 1). This method does not guarantee a positive  $v_{\phi}^2$ ; this must be checked *a posteriori* (see Melioli et al. 2008).

## 2.2 SFR and SN explosions

Dwarf irregular galaxies have generally low SFR, around few  $10^{-3} M_{\odot} \text{ yr}^{-1}$  (e.g. van Zee et al. 1997; Young et al.

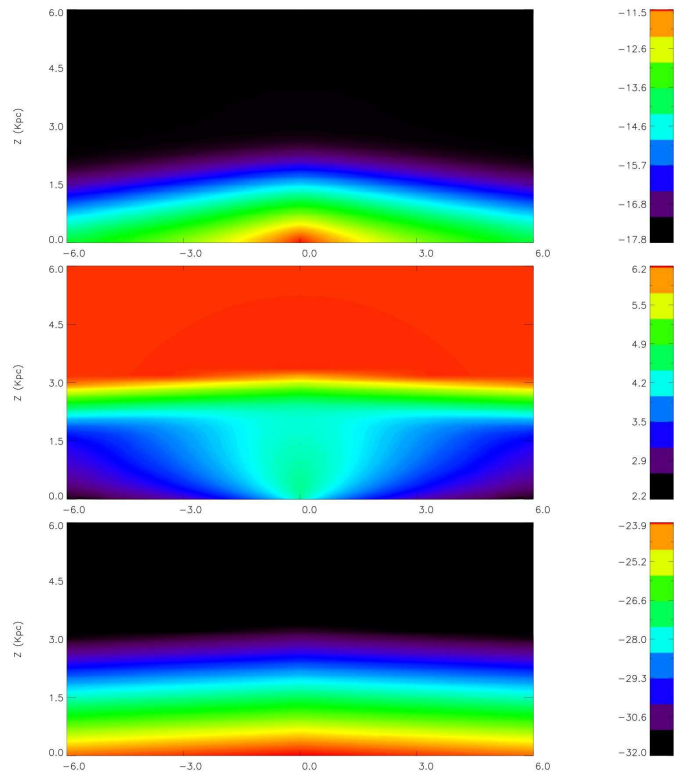


**Figure 3.** Edge-on logarithmic distribution of pressure (top panel), temperature (middle panel) and density (bottom panel) of the unperturbed ISM in our dwarf galaxy model. Distances are given in kpc and the horizontal axis represents either the  $x$  or the  $y$  axis crossing the galactic plane. Pressure, temperature and density have cgs units, logarithmic scale.

2003; Weisz et al. 2008; Lianou & Cole 2013). A large fraction of blue compact dwarf galaxies has instead a higher SFR ranging between  $10^{-3} M_{\odot} \text{ yr}^{-1}$  and several times  $10 M_{\odot} \text{ yr}^{-1}$ , with a median value of about  $0.1 M_{\odot} \text{ yr}^{-1}$  (e.g. Hopkins et al. 2002; Hunter & Elmegreen 2004; Zhao et al. 2011); the SF episodes can last for many hundreds of Myr (McQuinn et al. 2010, and references therein).

In order to reach a compromise between the computational cost of the simulations and the need of a numerical spatial resolution as high as possible, we consider the SF only in a limited region of the stellar disk, which we call the “active region”. This region extends up to  $R = 3 \text{ kpc}$ , enclosing 73% of the stellar mass.

We calculated three models. In the first one (MC1) we assume  $\text{SFR} = 7.3 \times 10^{-4} M_{\odot} \text{ yr}^{-1}$ , and a SF duration  $t_{\text{SF}} = 250 \text{ Myr}$ . In the second model (MC2) it is  $\text{SFR} = 7.3 \times 10^{-3} M_{\odot} \text{ yr}^{-1}$ , and  $t_{\text{SF}} = 120 \text{ Myr}$ . The specific SFR (SFR / stellar mass) of these two models is  $\sim 2 \times 10^{-12} \text{ yr}^{-1}$  and  $\sim 2 \times 10^{-11} \text{ yr}^{-1}$ , respectively. The former value is somewhat less than typical for dwarf irregulars, while the latter lies in the average range (Weisz et al. 2011).

The shorter duration of the stellar formation in MC2 is due to the fact that we inhibit the SF whenever the mean gas density on the galactic plane (where the stars are assumed to form) decreases below  $10^{-2} \text{ cm}^{-3}$ ; this never occurs in model MC1, where the SFR is low and the gas removal is less conspicuous, but it happens in model MC2 at about 120

**Table 1.** Galactic parameters.

$M_g$ $10^8 M_\odot$	$R_d$ kpc	$z_d$ kpc	$\Sigma_d$ $M_\odot \text{ pc}^{-2}$	$M_{\text{vir}}$ $10^8 M_\odot$	$r_{\text{vir}}$ kpc	$r_s$ kpc	$c_{102}$	$M_\star$ $10^8 M_\odot$	$R_{\star,t}$ kpc	$R_{\star,c}$ kpc	$z_{\star,t}$ kpc	$z_{\star,c}$ kpc
1.5	4	0.17	8	100	55.3	2.94	18.8	4	4.8	1.2	2.6	0.67

**Table 2.** Models parameters. The rates represent temporal mean estimates during the SN activity.

Model	SFR <sup>a</sup> $M_\odot \text{ yr}^{-1}$	SN rate $\text{yr}^{-1}$	SN luminosity $\text{erg s}^{-1}$	$E_{\text{inj}}^b$ erg
MC1	$7.3 \times 10^{-4}$	$7.3 \times 10^{-6}$	$2 \times 10^{38}$	$1.75 \times 10^{54}$
MC2	$7.3 \times 10^{-3}$	$7.3 \times 10^{-5}$	$2 \times 10^{39}$	$8.95 \times 10^{54}$
MC3	-	$7.3 \times 10^{-4}$	$2 \times 10^{40}$	$2.2 \times 10^{55}$

<sup>a</sup> The model MC3 has an instantaneous SF.

<sup>b</sup> Total energy released by the SNe during each simulation.

Myr. Of course, once the SNe stop to explode, a back filling of the ISM takes place increasing the gas density on the plane, and a second SF burst may arise. However, although we run all our models up to 250 Myr, we do not consider such a possibility. Finally, we also calculated a model MC3 in which the star formation is very short (hereafter indicated as instantaneous), and giving rise to  $\sim 2.2 \times 10^6 M_\odot$  of stars. The parameters of the different models are collected in Table 2.2.

The SN rate is derived from the assumed SFR as:  $\mathcal{R} = 0.01 \times \text{SFR} \text{ yr}^{-1}$ . This is close to the value expected for a Salpeter IMF with minimum and maximum star mass of 0.1 and  $100 M_\odot$ , respectively. For the model MC3, where the SFR is instantaneous, we assume that the SNe explode over a timescale of  $t_{\text{exp}} = 30$  Myr, which is the lifetime of a  $8 M_\odot$  star, the least massive SN progenitor star. Thus, the average SN rate is  $(0.01 \times 2.2 \times 10^6) / (3 \times 10^7) = 7.3 \times 10^{-4} \text{ yr}^{-1}$  for  $t \leq 30$  Myr, and zero otherwise (see Table 2.2).

We note here that the three assumed SN rates are not inconsistent with the observed SFR-surface density relation. Given our assumption of 1 SN every  $100 M_\odot$  of newly formed stars, on the basis of the Kennicutt-Schmidt (KS) relation the expected SN rate is (Kennicutt 1998)

$$\dot{\Sigma}_{\text{SN}} \simeq 2.5 \times 10^{-6} \Sigma_{\text{g1}}^{1.4} \text{ yr}^{-1} \text{ kpc}^{-2}, \quad (4)$$

where  $\Sigma_{\text{g1}} \equiv \Sigma_{\text{g}} / 1 M_\odot \text{ yr}^{-1}$  is the gas surface density. Taking  $\Sigma_{\text{g}} \sim 5.5 M_\odot \text{ yr}^{-1}$  as the average value within the active area, it turns out that the SN rate should be  $\sim 7.7 \times 10^{-4}$ , similar to the rate of model MC3. Even the lower rates of models MC1 and MC2 are compatible with the observed steepening and dispersion of the KS relation at low gas surface densities (e.g. Roychowdhury et al. 2009; Shi et al. 2011). This consistency is not surprising, given that the assumed SFRs lie among the observed range for dwarf galaxies (see above).

We neglect the supernovae Ia (SNeIa) contribution from both the energetic and chemical point of view. Their number is less than half of that of SNeII (Mannucci et al. 2005), and the amount of oxygen ejected (the element we are interested in, as a tracer of the  $\alpha$ -elements) is negligible (e.g. Marcolini et al. 2007, and references therein).

We assume that stars form randomly in time and

space, mostly within stellar associations of different mass  $M_{\star,\text{cl}}$  (Ward-Thompson 2002), each generating a total number of SNe  $N_{\text{SN}} = 0.01 \times M_{\star,\text{cl}} / M_\odot$ . As in Melioli et al. (2009), we assume that the cluster distribution is given by (Higdon & Lingenfelter 2005)  $f(N_{\text{SN}}) \propto N_{\text{SN}}^{-2}$ , where  $f(N_{\text{SN}}) dN_{\text{SN}}$  is the number of stellar clusters with the number of SN progenitors between  $N_{\text{SN}}$  and  $N_{\text{SN}} + dN_{\text{SN}}$ . This distribution is assumed to be valid in the range  $N_{\text{min}} < N_{\text{SN}} < N_{\text{max}}$ , with  $N_{\text{max}} = 300$ , while for numerical reasons the value of  $N_{\text{min}}$  depends on the model (see below).

The stars within each cluster are supposed to be coeval, so that the SNe occur sufficiently close to each other in time and space to interact mutually, forming a single superbubble. We therefore consider each association as a single source injecting energy and mass for  $t_{\text{exp}} = 30$  Myr after the cluster formation at a constant rate of  $L_w = E_0 N_{\text{SN}} / t_{\text{exp}}$  and  $\dot{M} = M_{\text{ej}} N_{\text{SN}} / t_{\text{exp}}$ . Here  $M_{\text{ej}} = 16 M_\odot$  and  $E_0 = 10^{51}$  erg are the mean mass and energy released by a single explosion, respectively (Marcolini et al. 2007, and references therein).<sup>1</sup>

A number of clusters are randomly extracted from the distribution  $f(N_{\text{SN}})$ , until a total number of supernovae  $\mathcal{R}_{\text{TSF}}$  is obtained. In order to place the clusters in space and time each  $i$ -th cluster is randomly associated to a position  $P_i$  on the galactic plane ( $z=0$ ) at a random time  $t_i$  in the interval  $0 < t_i < t_{\text{SF}}$ . The procedure generates random points with a spatial frequency proportional to the stellar density described by equation 1. If, however, the  $i$ -th cluster happens to be located at distances smaller than 80 pc from a previous association whose SN activity terminated since less than 60 Myr, its position is recalculated; this is because we assume that the SN wind of the previous cluster clears the local volume of its gas, preventing any further SF for a while.

The above procedure influences the choice of  $N_{\text{min}}$ . In principle it can be as low as  $N_{\text{min}} = 1$ , but in model MC1 we assume  $N_{\text{min}} = 5$  because with the disk initial conditions assumed here, a superbubble can breakout only when  $L > L_{\text{cr}} \sim 6 \times 10^{36} \text{ erg s}^{-1}$  (Koo & McKee 1992), which corresponds to  $N_{\text{SN}} = 5$ . However, when the number of OB associations is high, after a while the procedure described in the previous paragraph hardly allows to place a new OB association, as they are too close in space and time. For this reason in MC2 we assume  $N_{\text{min}} = 20$ ; in so doing we reduce the number of sampled clusters. This strategy is physically meaningful; in fact, as the smaller associations are more numerous, the bubbles they form easily merge producing effects similar to those due to larger OB associations. We finally point out that in model MC3 we again assume

<sup>1</sup> We neglect the stellar wind energy of the SN progenitors, as it makes only a minor contribution in the total mechanical energy budget, especially for a metal poor stellar population relevant for dwarf galaxies (see Leitherer et al. 1999).

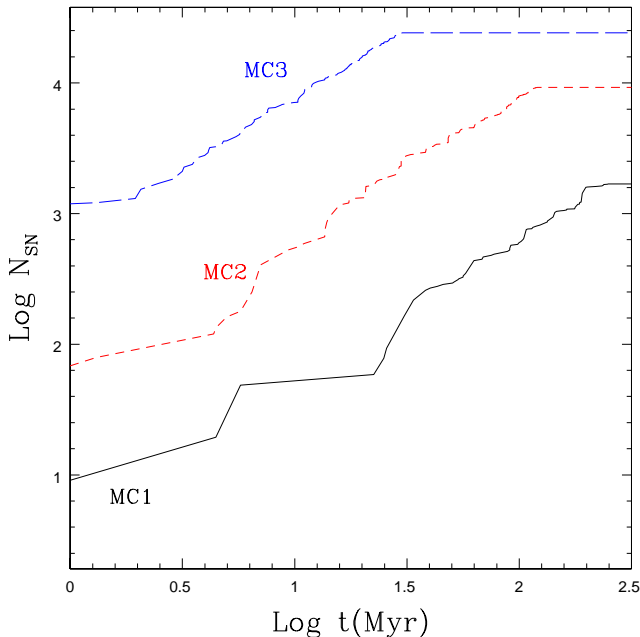


**Figure 4.** Cumulative number of supernovae for the three models.

$N_{\min} = 5$  as all the clusters are located essentially at the same time. This variation in  $N_{\min}$  among the three models might have a small impact on the results, since it results in a change of the star clusters spatial density which is not strictly proportional to the SN rate.

The cumulative number of SNe with time for the three models is illustrated in Figure 4.

### 2.3 Numerics

The simulations are calculated using a modified version of the adaptive mesh refinement hydrodynamical code YGUAZU (Raga et al. 2000) that integrates the gas-dynamic equations using the *flux vector splitting* algorithm of van Leer (1982). Radiative losses are taken into account by an analytic fit to the cooling curve given by Sutherland & Dopita (1993) as a function of the temperature  $T$  and metallicity  $Z$  for  $T \geq 10^4$  K; for  $T < 10^4$  K we assume the cooling curve given by Dalgarno & McCray (1972). With a highest resolution of 20 pc (see below) the initial phase of superbubble expansion is not accurately simulated. In particular, the radiative losses would be greatly overestimated due to the numerical diffusion which generates large spurious regions of gas at intermediate temperatures and density at the boundary between the shocked SN ejecta and the shocked ISM. To mitigate this effect we artificially reduce the cooling term near the galactic plane. At  $z = 0$  it is only 5 % of the real value, and gradually increases with the height  $z$  to reach the full value for  $z = 300$  pc. We believe that this “trick” protects our simulations from spurious overcooling while allowing an accurate description of the flow on large scale, which is the main purpose of this paper. We further investigate the effect of radiative cooling in the Appendix A.

The 3-D eulerian adaptive hierarchical numerical grid has five levels of refinements with mesh sizes of 320 pc, 160 pc, 80 pc, 40 pc and 20 pc, respectively. The two coarser grids cover the whole computational box  $-5.2 < x < 5.2$ ,  $-5.2 < y < 5.2$ ,  $0 < z < 10.4$  kpc, while the finest one extends up to  $-3 < x < 3$  kpc,  $-3 < y < 3$  kpc and  $z = 160$  pc, the next one up to  $-3.84 < x < 3.84$  kpc,  $-3.84 < y < 3.84$  kpc,  $0 < z < 1.28$  kpc, and the remaining one  $-5.2 < x < 5.2$  kpc,  $-5.2 < y < 5.2$  kpc,  $0 < z < 3.84$  kpc. In this study the different grid levels are enforced altogether at any time. A convergence test is presented in Appendix B.

As the grid encompasses only the “upper half” ( $z > 0$ ) of the galaxy, outflow boundary conditions are enforced at every grid edge but the galactic plane ( $z = 0$ ), where reflecting boundary conditions are applied. This latter constraint requires that the SN events must be located on the mid-plane; as a consequence we inject into the grid only half of the mass and energy released by the SNe, as the other half should be introduced into the “ghost” half of the galaxy. A passive tracer is also added to track the SN ejecta.

The SN energy injection is purely thermal. Because the numerical grid is at rest in space while the Galaxy rotates, each OB association occurring in the active area moves along a circle on the  $z = 0$  plane. At each time, we place the energy and mass sources in a single cell of the finest grid transited by the association at that time.

## 3 RESULTS

In this Section we focus mainly on the dynamics of the ISM and the SN ejecta. More quantitative discussions on the mass and energy budget and the chemical enrichment process is postponed to Section 4.

In the following we divide the galaxy in two regions: the *disk*, defined as the volume within  $R < 5$  kpc,  $z < 500$  pc, and the region of space outside the disk, that for simplicity we call “halo”. This separation allows us to characterize the enrichment of the stellar body, where new stars are formed, and that of the intergalactic medium (IGM).

For future reference (see Section 4) we point out that the initial amount of unperturbed ISM of the disk within the grid is  $M_{g,0}^{\text{disk}} \sim 1.4 \times 10^8 M_{\odot}$ , while the remaining gas with mass  $M_{g,0}^{\text{halo}} \sim 10^7 M_{\odot}$  is distributed within the halo.

### 3.1 MC1

In the first model (MC1) we assume a continuous mean SFR of  $7.3 \times 10^{-4} M_{\odot} \text{ yr}^{-1}$  within the active region, corresponding to an average SN rate of  $7.3 \times 10^{-6} \text{ yr}^{-1}$  within the active region. This simulation lasts  $\sim 250$  Myr, and  $\sim 1750$  SNe explode in this time interval. The SNe are clustered in 69 different stellar associations distributed following the power law given in Section 2.2.

#### 3.1.1 ISM evolution

The first row of Figure 5 illustrates the face-on ISM column density (calculated for  $0 < z < 500$  pc, that is within the disk thickness) distribution at different times. The holes created by the SN activity tend to acquire an elongated shape due to the differential rotation of the galaxy. In general, the

largest holes are created in the outskirts of the active region, where the ISM is more easily removed owing to its lower density and pressure. Given the low SN rate, the filling factor of the bubbles powered by the SN associations is rather small, and the holes created by the explosions do not produce a coherent action of gas removal.

Yet, Figure 6 shows that SN clusters can lift gas well above the disk, although never beyond the grid top boundary. The filaments and the bubbling structure seen in this figure are the result of the interaction among shells of the cavities produced by the single SN clusters. As pointed out above, the low frequency of the intermittent SN activity prevents an effective synergy among different bubbles. As a result, while the hot tenuous ejecta within single bubbles is energized enough to be thrown upward with velocities that can reach a few hundreds of  $\text{km s}^{-1}$ , the colder and denser ISM filaments, more resilient to be accelerated, acquire velocities which hardly rise to  $100 \text{ km s}^{-1}$ . This is illustrated in Figure 7 which shows the mass-weighted distribution of gas vertical velocity. Anticipating the definition given in Section 4.4, in this figure two gas phases are considered: a hot phase with  $T \geq 10^5 \text{ K}$ , and a cold one with  $10^2 < T < 10^5 \text{ K}$ . At any time the cold gas moves in the  $z$ -direction with a velocity  $v_z < \sim 85 \text{ km s}^{-1}$ , lower than the local escape velocity. The hot gas velocity distribution, instead, develops a high velocity tail. The different behaviour of the cold phase, representative of the star forming ISM, and of the hot phase, which contains most of the recently produced SN metals, is crucial in the chemical evolution of the galaxy (cf. Section 5).

### 3.1.2 SN ejecta distribution

Figures 8 and 9 show the column density of the SN ejecta along the  $z$  direction in the range  $0 < z \leq 500 \text{ pc}$  and  $z > 500 \text{ pc}$ , respectively. These maps nicely illustrate the circulation of the metals due to the SN feedback. The SN ejecta spatial distribution within the disk quickly becomes inhomogeneous, with column density variations of 5 – 10 between nearby regions (middle panel, top row of Figure 8). With time, rotation and hydrodynamical dispersal tend to erase azimuthal fluctuations, leaving a centrally concentrated metal distribution. In the halo, instead, the SN ejecta has still an irregular distribution at the final time of the simulation ( $t = 250 \text{ Myr}$ ). In Figure 7 it is shown that only a tiny fraction of the (hot) gas is fast enough to leave the system. Evidently, the weak SF feedback of model MC1 is only able to lift some fraction of the SN metals in the halo, where they spread over a large volume. The chemical enrichment process will be discussed in detail in Section 4.

### 3.2 MC2

In this model the average SN rate is  $7.3 \times 10^{-5} \text{ yr}^{-1}$ , an order of magnitude higher than in MC1. The occurring 8945 SNe are clustered in 158 different stellar associations.

As can be seen in column density map (Figure 5), the galactic ISM on the disk appears soon punched by holes, which then mostly merge, clearing the active area of the original ISM. The single bubbles created by different SN clusters incorporate each other, and their combined action

produces a galactic wind strong enough to lift the ISM to large heights as can be seen in Figure 6. An almost steady high-velocity tail develops in the velocity distribution of the hot component, and even the distribution of the cold ISM extends beyond  $\geq 250 \text{ km s}^{-1}$  at  $t \sim 100 \text{ Myr}$  (see Figure 7), well above the escape velocity. The ISM is then vented in the halo and some of it is able to leave the system, moving through the upper grid boundary. Contrary to model MC1, the SN ejecta is also moved to higher values of  $z$ , as can be qualitatively understood comparing the column densities in the range  $0 < z \leq 500 \text{ pc}$  and  $z > 500 \text{ pc}$  (middle rows in Figures 8 and 9, respectively). Analogously to (and more appreciably than in) model MC1, the ejecta in the halo expands all over the galaxy.

In conclusion, the SNe essentially remove the ISM close to the equatorial plane. When this happens, at  $t \sim 120 \text{ Myr}$ , we stop the SN explosions, consistently with the assumption that the star formation process is quenched. We evolved the simulation further, however, in order to follow the ISM settlement after the SN activity. The holes generated by such activity shrink in about a sound crossing time. The disk recovers almost all the gas that was lifted up or pushed radially, retrieving up to 90% of the initial mass at  $t = 250 \text{ Myr}$ , after 130 Myr since the SN explosions terminated (cf. Section 4). The dynamical effect of the SF is still observable in the persistent presence of spiral features in the ISM, as shown in Figure 5. During the quiescent time only a fraction of the ejecta floating into the halo slowly falls back, while the rest moves outside the computational grid. The time evolution of the spatial distribution of the ejecta column density is depicted in Figures 8 and 9. As for model MC1, significant metal inhomogeneities are present both in the disk and in the halo, especially during the SF phase. While in the disk the metal pollution is limited to the active region, in the halo the SN ejecta reaches larger radial distances.

### 3.3 MC3

In this model we consider an instantaneous event of star formation, in which  $\sim 3 \times 10^6 M_{\odot}$  of stars form. The corresponding SN rate is  $7.3 \times 10^{-4} \text{ yr}^{-1}$  (c.f. Section 2.2). We have therefore  $\sim 22000$  SNe injecting an average luminosity  $L_{\text{SN}} \sim 2.2 \times 10^{40} \text{ erg s}^{-1}$  in a time interval of 30 Myr.

At the beginning, the large number of hot bubbles and the amount of injected energy are able to disrupt the ISM in the central region of the galactic plane. Part of the gas is compressed and pushed sideways, as shown in the first panel of the third row of Figure 5, where the holes appear to be limited by dense rims. A large fraction of the hot gas acquires vertical velocities much larger than the escape velocity (cf. Figure 7); this gas leaves the galaxy and crosses the upward boundary of the computational box (cf. Figure 6).

At the end of the SN activity, the gas in the dense shells generated by the superbubbles expansion rushes toward the central region on about a sound crossing time ( $\sim 200 \text{ Myr}$ ). At  $t = 100 \text{ Myr}$  some holes are still present (see middle panel of the bottom row in Figure 5). At later time the galaxy is able to re-grow its gaseous disk, as some of the ISM previously lifted in the halo rains back toward the galactic plane (see 5). An analogous consideration holds for the SN ejecta, as it is apparent comparing the last two panels of Figure 8 with those of Figure 9: in fact, while the ejecta



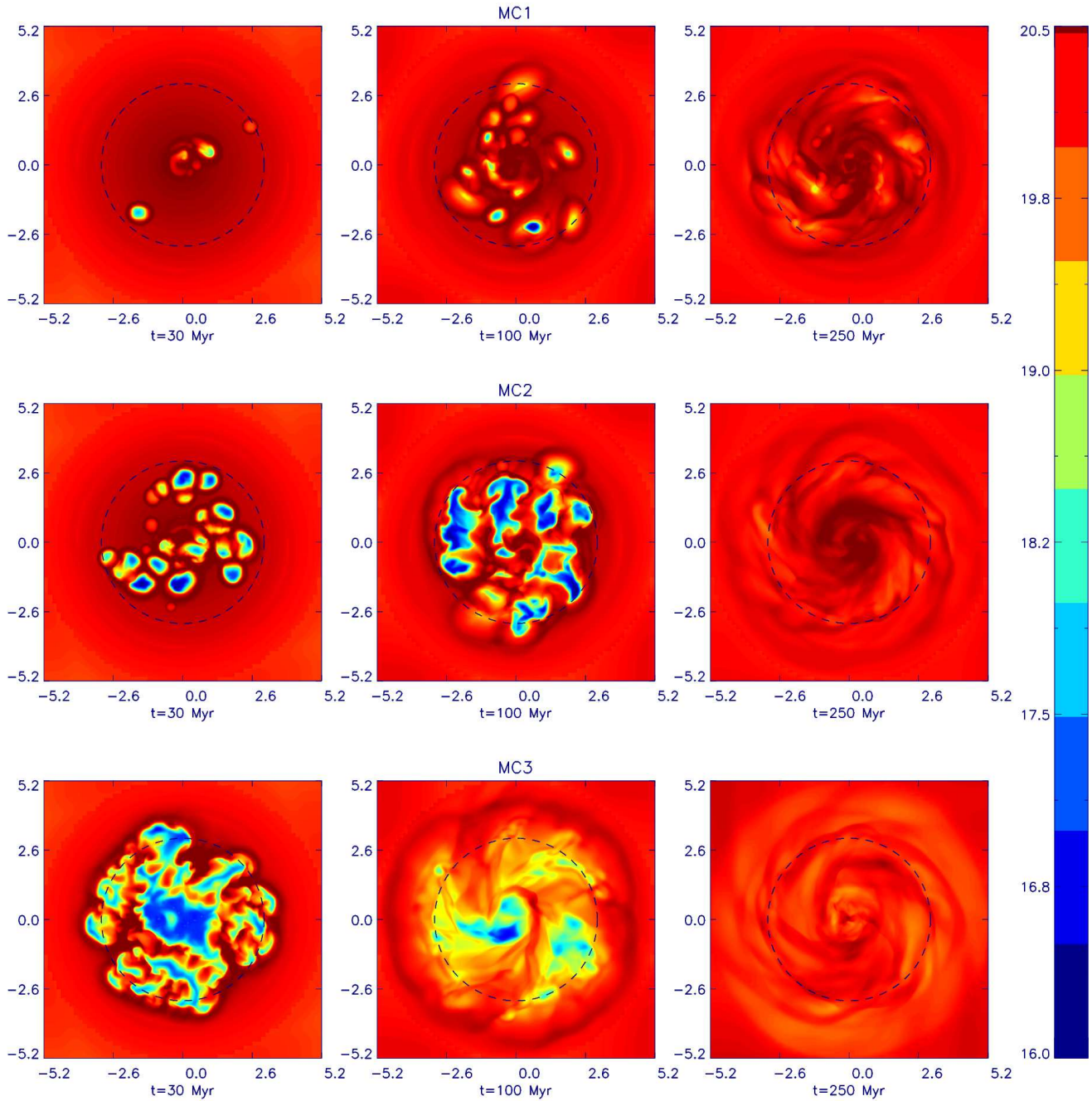


**Figure 5.** Distribution of the face-on gas column density (for  $0 < z < 500$  pc). Each row refers to a single model. Each column refers to a single time. The dashed circle delimitates the active area (see text). Distances are in kpc and the (horizontal) x-axis and (vertical) y-axis individuate the galactic plane. Column densities are in  $\log(\text{g cm}^{-2})$  units.

column density in the disk at  $t = 100$  Myr is generally lower than at  $t = 250$  Myr, the opposite is true for the halo.

As for model MC2, also in this case the SN explosions create spiral (gas) density waves, still present at  $t = 250$  Myr.

## 4 DISCUSSION

### 4.1 ISM mass budget

Figure 10 compares the temporal evolution of the ISM content within the disk and the halo for the three models.

In model MC1 the gas involved in the SN feedback circulation belongs almost entirely to the active area, as also indicated by Figure 5. After 250 Myr the disk loses only  $\sim 6\%$  of the initial amount of ISM. Comparing the two panels of Figure 10, one sees that this gas is simply lifted into

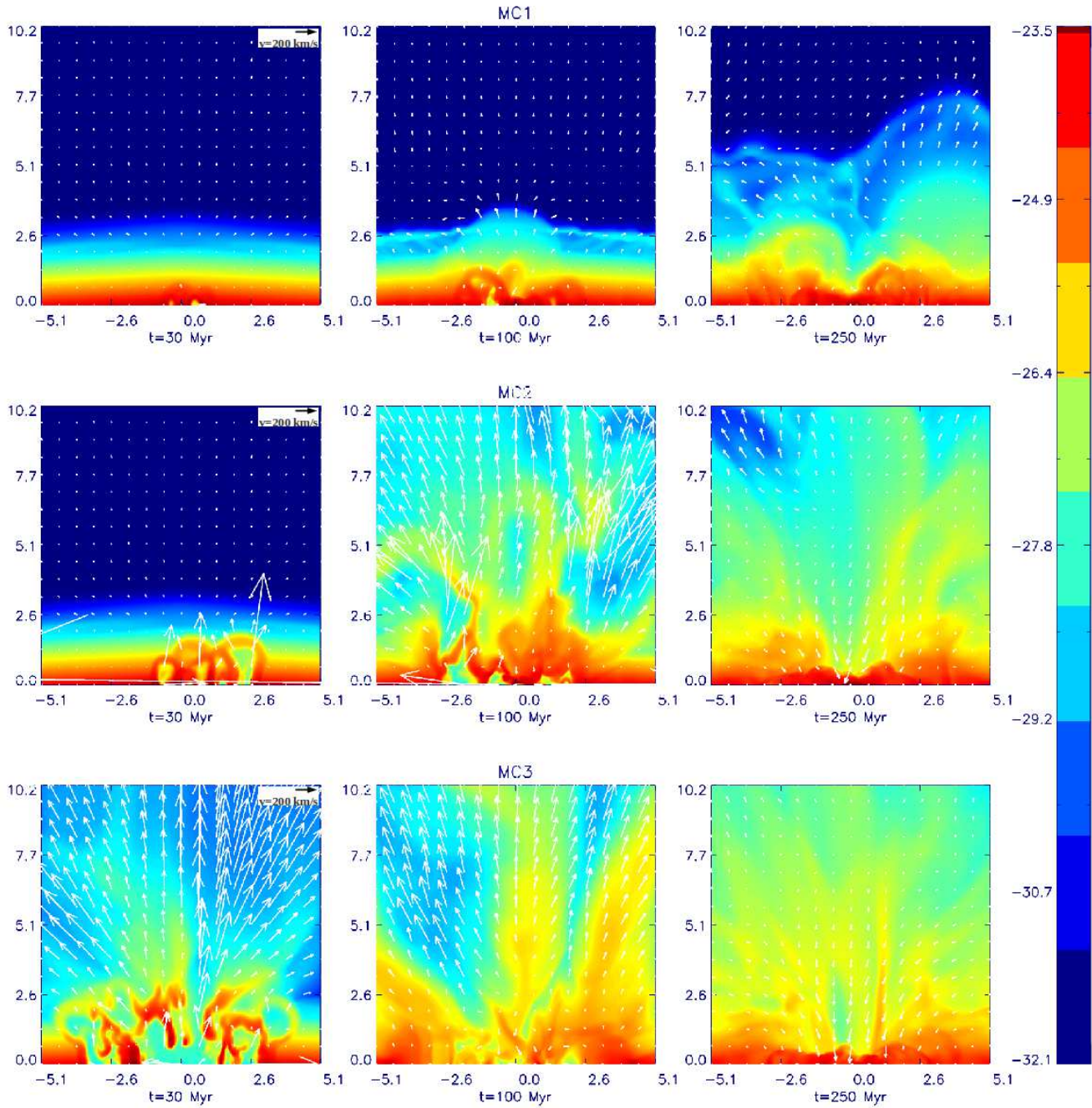


**Figure 6.** Gas density distribution on the  $x = 0$  plane (edge-on view). Each row refers to a single model. Each column refers to a single time. The arrows illustrate the velocity field. Distances are in kpc and the (horizontal)  $x$ -axis and (vertical)  $z$ -axis individuate the plane perpendicular to the galactic disk at  $R=0$ . Densities are in  $\log(\text{g cm}^{-3})$  units.

the halo, and is not lost from the system, as anticipated in Section 3.1.

Because of the higher SN rate, in model MC2 the disk loses a larger fraction of ISM. The disk gas flows into the halo at an average rate of  $\sim 0.3 M_{\odot} \text{ yr}^{-1}$ , up to the end of the SN activity, occurring at  $t = 120$  Myr. At this time the disk has lost about 30% of its initial gas content. In the same period the gas in the halo increases, reaching a maximum at  $t = 120$  Myr. After the star formation is halted, the amount of gas in the disk starts to grow, recovering 85% of its initial value

at  $t = 250$  Myr. From the symmetric shape of the dashed curves in the two panels of Figure 10 (and from their values) it turns out that, as for the model MC1, almost all the gas lost by the disk is transferred into the halo where it remains bounded to the galaxy. When the action of the SNe ceases, this gas falls back onto the disk at an average rate of  $\sim 0.15 M_{\odot} \text{ yr}^{-1}$ . At  $t = 250$  Myr only 2% of the total initial ISM has been lost.

As expected, the disk of model MC3 suffers the largest and fastest ISM removal because of the higher SN rate. In-



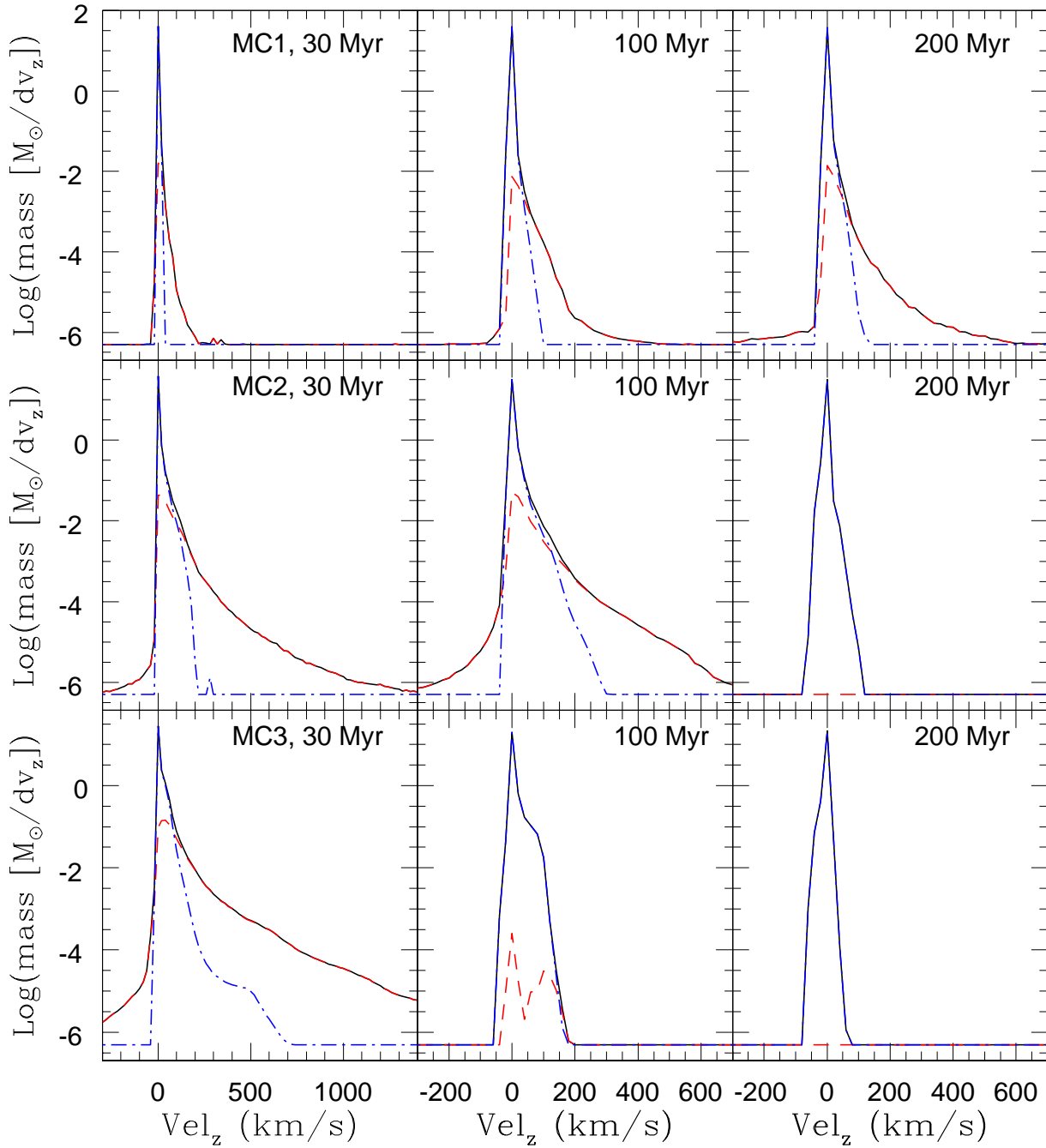


**Figure 7.** Mass-weighted distribution of gas vertical velocity. The dot-dashed line refers to the cold phase ( $10^2 < T < 10^5$  K), the dashed line refers to the hot phase ( $T > 10^5$  K), and the solid line refers to the whole gas. Each row refers to a single model. Each column refers to a single time.

terestingly, the disk gas outflow persists well beyond the SN quenching (occurring at 30 Myr). In fact, the galactic-scale shock wave, generated by the cumulative effects of the SN explosions, propagates laterally through the galactic plane (and also above it) and keeps expanding up to more than 100 Myr, as apparent by the rim present in the second panel of the third row of Figure 5 encircling the area perturbed by the SN activity. As a consequence, the ISM on the plane is lifted up by this shock, and pushed toward the grid boundaries. After an initial rapid increase, the amount of gas within

the halo stays approximately constant (cf. Figure 10). In fact, the SN energy release is not spatially homogeneous, and different funnels form, through which hot and rarefied gas (ISM and SN ejecta) is channeled upward. The walls of the funnels, on the other hand, collide each other, becoming denser and colder because of the increased radiative cooling due to the compression. Their rising motion is thus greatly slowed down and, as a result, they remain bounded to the galaxy, floating a long time within the halo, as apparent in the last two panels of the bottom row of Figure 6. As most

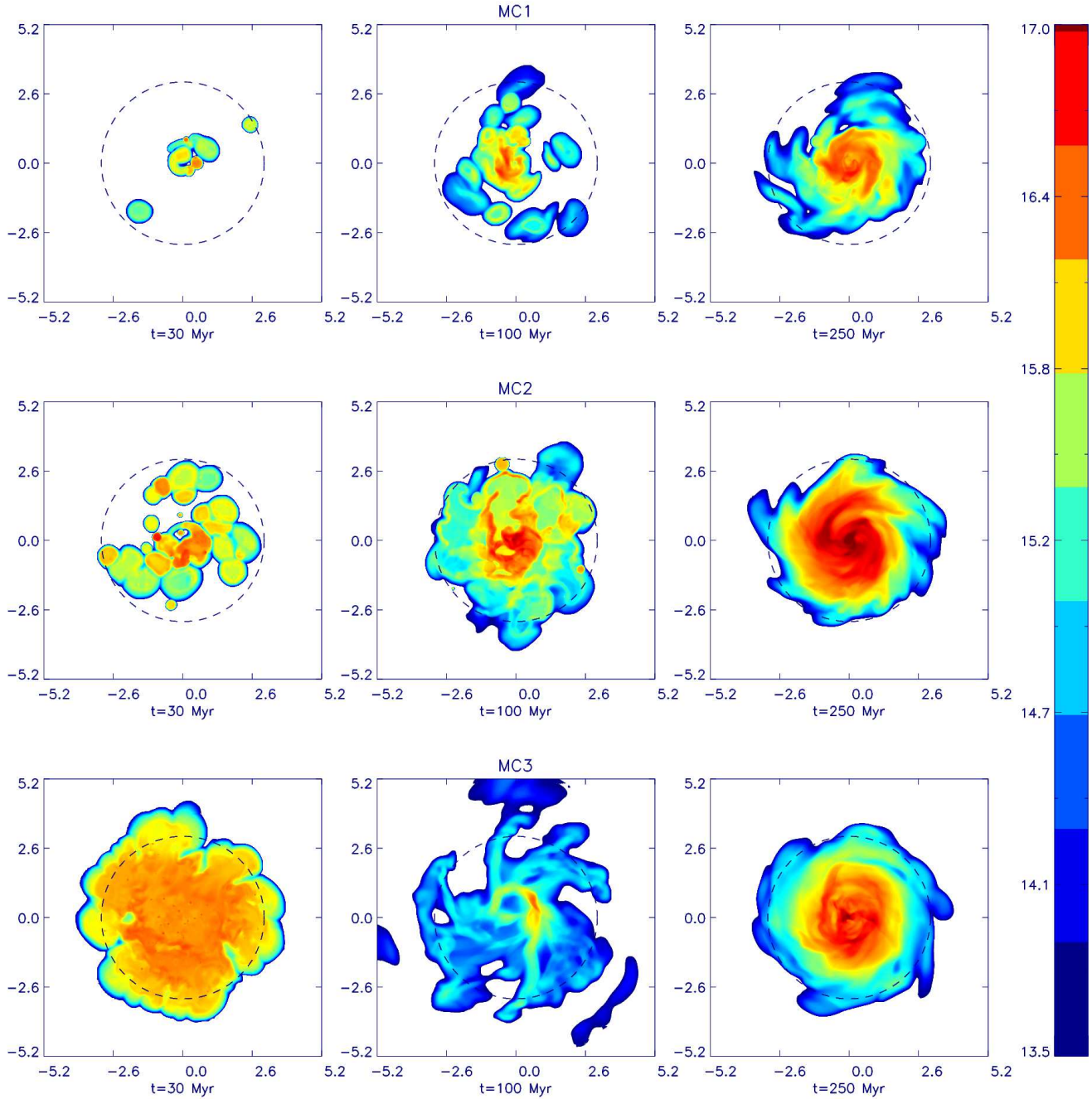


**Figure 8.** Column density of the SN ejecta along the  $z$ -direction in the range  $0 < z \leq 500$  pc. Each row refers to a single model. Each column refers to a single time. The dashed circle delimitates the active area (see text). Distances are in kpc and the (horizontal)  $x$ -axis and (vertical)  $y$ -axis individuate the galactic plane. Column densities are in  $\log(\text{g cm}^{-2})$  units.

of the halo gas is concentrated within the walls, its total amount does not vary at this stage, as shown in Figure 10. At  $t \sim 170$  Myr some of the gas of the halo starts to move back onto the disk. After 250 Myr the gaseous disk contains 50% of the initial ISM, while about 40% of it is found in the halo. Only  $\sim 1.4 \times 10^7 M_{\odot}$  of gas have crossed the grid boundaries and left the system. This is less than 10% of the total amount of gas initially present in the computational box.

Despite the absence of substantial ISM removal, in mod-

els MC2 and MC3 the SN feedback significantly alters the distribution of the ISM between the disk and the halo. An important result is the formation of massive multiphase “extra-planar” gas, located at height  $z > 500$  pc. This halo gas, generated by the SN action, lasts for several  $10^8$  yr and is analogous to the extra-planar gas generated by galactic fountain in massive spiral galaxies (Melioli et al. 2009, and references therein).

In conclusion, all the three models retain almost all the initial ISM. This may be somewhat surprising, as in mod-

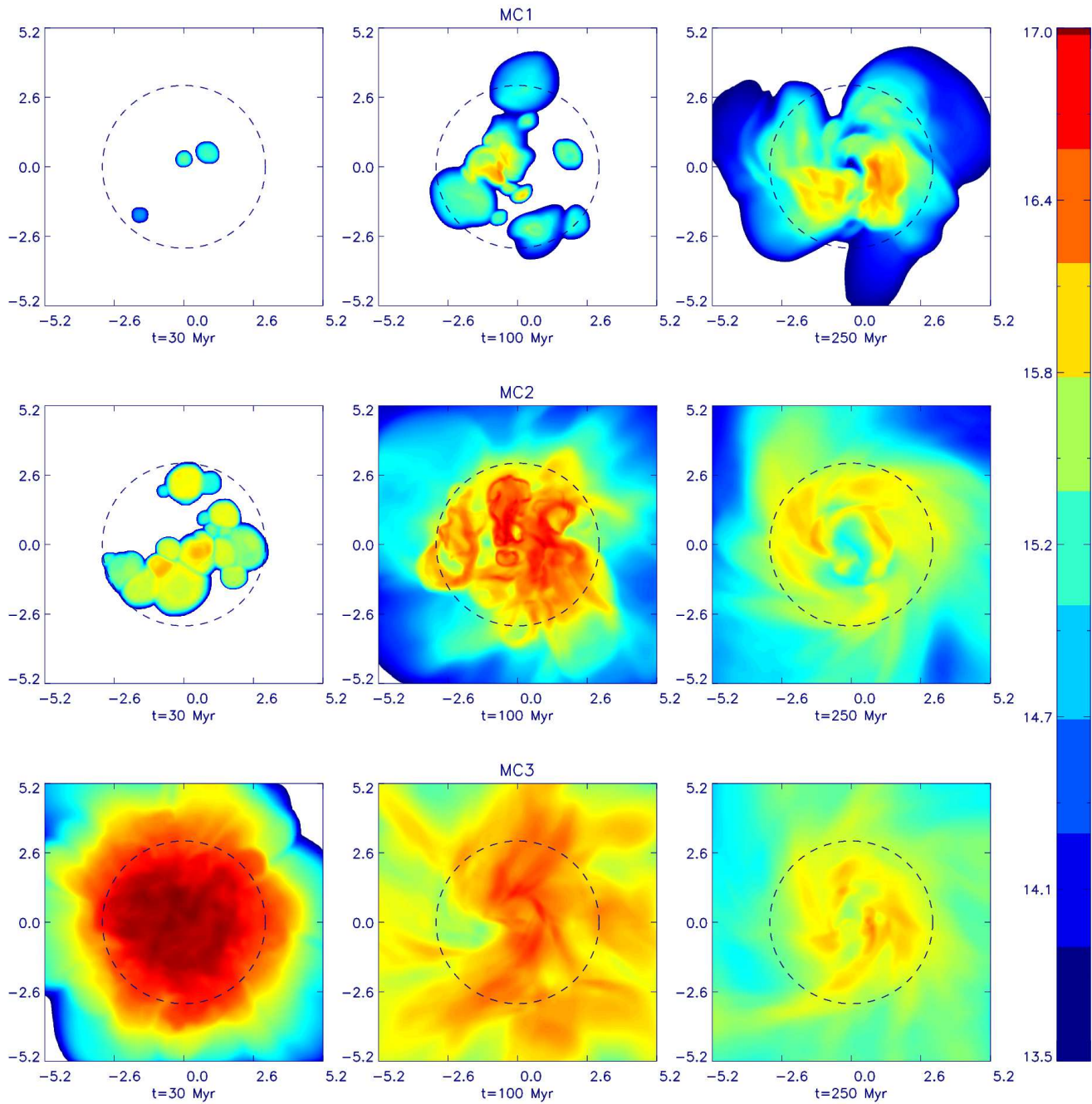


**Figure 9.** Column density of the SN ejecta along the  $z$ -direction for  $z > 500$  pc. Each row refers to a single model. Each column refers to a single time. The dashed circle delimitates the active area (see text). Distances are in kpc and the (horizontal)  $x$ -axis and (vertical)  $y$ -axis individuate the galactic plane. Column densities are in  $\log(\text{g cm}^{-2})$  units.

els MC2 and, especially, MC3 the total energy delivered by the SNe (cf. Table 2.2) is comparable with the ISM binding energy,  $E_{\text{bind}} \sim 3.6 \times 10^{55} \text{ erg}^2$ . We discuss this point in Section 4.3. This result is strengthened by the convergence test presented in Appendix B. There we show that the disk

mass content is not strongly sensitive to the spatial resolution, slowly increasing with the grid refinement. Therefore the disk gas masses quoted in this Section should be taken as lower limits.

<sup>2</sup> Previous works have shown that SNe may substantially fail in ridding the ISM even if their energy is much larger than the gas binding energy (e.g. D’Ercole & Brighenti 1999; Marcolini et al. 2006, and references therein).

## 4.2 Ejecta mass budget

As discussed in Section 3, the fate of the SN metals is rather different from that of the ISM. Figure 11 shows the evolution

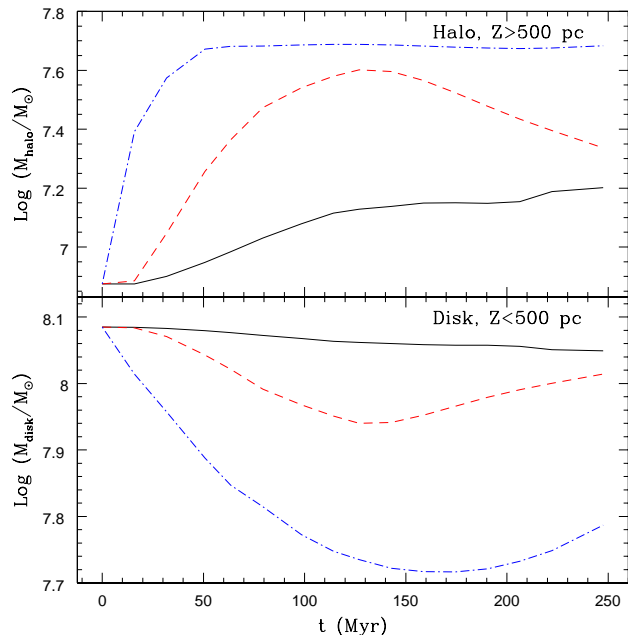


**Figure 10.** Upper panel: time evolution of the mass of gas within the halo ( $z > 500$  pc) for the models MC1 (solid line), MC2 (dashed line) and MC3 (dot-dashed line). Bottom panel: as the upper panel, but for the disk ( $z < 500$  pc).

of the SN ejecta mass (normalized to the total ejecta released at a given time) in the disk and in the halo.

At early times the freshly delivered ejecta in model MC1 is found mainly in the disk. With time, however, the fraction of the ejecta present into the halo increases at the expense of the fraction contained within the disk; after 100 Myr an almost steady configuration is established, in which the amount of new ejecta lunched upward is approximately compensated by the ejecta in the halo which tends to move back onto the disk. The relative amounts of ejecta below and above 500 pc then change rather slowly and, after 250 Myr, are both to  $\sim 50\%$ , showing that the most of the metals shed by the SNe are retained by the galaxy.

As long as SNe are active ( $t \leq 120$  Myr), the behaviour of the ejecta in model MC2 is qualitatively similar to that found in model MC1. Initially, when the amount of the SN ejecta is still quite small, the ejecta itself is mostly found into the disk; however, after only  $\sim 30$  Myr, its quantity in the halo is about 40% of the total. This percentage keeps increasing as long as the SNe explode, reaching the maximum value of  $\sim 70\%$ ; such fraction is larger than in model MC1 because of the higher SN rate of model MC2. Once the SNe stop, the ejecta in the halo starts to fall back onto the disk where its amount increases, in pace with the behaviour of the ISM (cf. Figure 10). At the end of the simulation, the quantity of ejecta within the whole galaxy is  $\sim 75\%$  of the total, an evidence that a large fraction of it ( $\sim 25\%$ ) has been lost by the galaxy.

For model MC3 the SN feedback has a more dramatic impact. The SN rate is so high that, after 30 Myr (the end of the SN activity) 80% of the ejecta has been already transported above the disk. After this time the ejecta leaves the

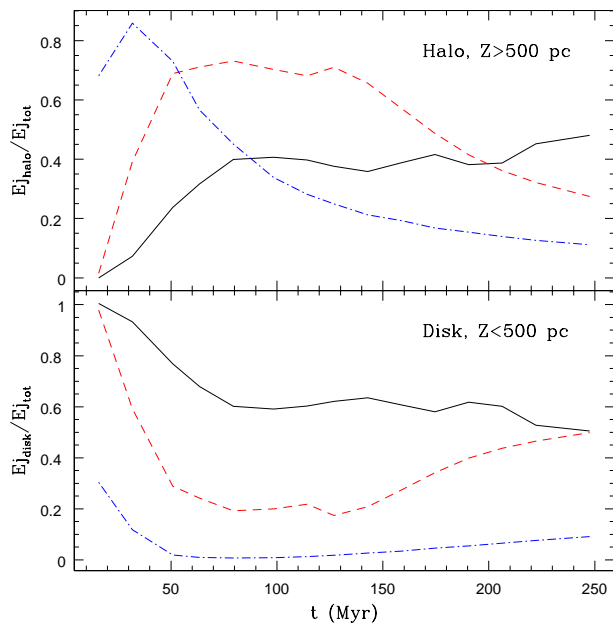


**Figure 11.** Upper panel: time evolution of the amount of SN ejecta within the halo for the models MC1 (solid line), MC2 (dashed line) and MC3 (dot-dashed line). Lower panel: as the upper panel, but for the disk. At each time the masses are normalized to the mass injected by the SNe until that time. In order to go back to the absolute values, we report the normalization values at some representative times: at times  $t = \{50, 100, 150, 200, 250\}$  Myr the normalization values are  $M = \{4700, 10960, 16640, 22230, 27780\} M_{\odot}$  for MC1; at  $t = \{50, 100, 150\}$  Myr  $M = \{61640, 122520, 141240\} M_{\odot}$  for MC2; after  $t = 30$  Myr  $M = 383000 M_{\odot}$  for MC3.

halo, with only a tiny fraction of it moving back onto the disk, as shown in the lower panel of Figure 11. Therefore, in this model nearly 80% of the SN metals are lost into the surrounding IGM, showing that even dwarf galaxies with moderate SFR are able to enrich the IGM on scales larger than 10 kpc.

### 4.3 Energy budget and SN feedback

In order to evaluate the effectiveness of the SN feedback, it is interesting to compare the total energy released by the stellar explosions to the binding energy of the ISM,  $E_{\text{bind}} \sim 3.6 \times 10^{55}$  erg. From Table 2.2 we see that  $E_{\text{inj}}/E_{\text{bind}} = 0.05, 0.25, 0.61$  for models MC1, MC2 and MC3, respectively. The fraction of lost SN ejecta depends on the injected energy, its value being 0.0, 0.25, 0.80 for the same three models, respectively. On the contrary, no ISM leaves the galaxy, even in the most powerful model MC3. These results show that simplistic energy arguments may be misleading in determining the effect of the SN feedback.

Not all the SN energy goes in fact in venting away the local ISM. As discussed in Section 4.1, once the bubbles powered by the SN associations break out of the galactic plane, channels form (cf. Figure 6) along which the hot (metal rich) gas is conveyed into the halo and can leave the galaxy. This is apparent in Figure 7 where the high velocity tail



present in the velocity distribution during the SF phase is due to the hot gas carrying away a fraction of the SN energy in the form of thermal and kinetic energy; this energy is thus not available for removing the ISM. We stress that the initial distribution of the ISM plays an important role. Spherical ISM distributions (presumably the case in dwarf spheroidal galaxies), make break-outs more difficult to occur, and most of the SN ejecta could remain trapped within the ISM (Marcolini et al. 2006); the gas circulation would then be mainly regulated by the radiative cooling.

In this case the competition between the rate of the radiative losses and the rate of the energy injection (by SNe in our models) represents the key factor regulating the amount of ISM lost by the galaxy. If the injection rate is low compared to the rate of radiative losses, little gas is lost by the galaxy, even if the total amount of energy supplied by the SNe during their activity is higher than the binding energy of the ISM<sup>3</sup>. This is the reason why our models retain most of their ISM while, for instance, the model “SMC” of Hopkins et al. (2012), similar in mass, but with an higher SN rate, suffers a larger mass loss.

#### 4.4 Chemical enrichment and abundance gradients

One of the main aims of this study is to understand whether the SN explosions are able to spread the ejected metals over the whole disk, removing or modifying the intrinsic abundance gradient (given by the radial distribution of the stars and the ISM — cf. Figure 2).

To this end, at any radius  $R$  we have computed the disk gas metallicity (measured by  $12 + \log(\text{O}/\text{H})$ ) defined as the ratio between the azimuthal average of the oxygen and ISM column densities within cylindrical shells of radius  $R$  and thickness  $dR = 20$  pc<sup>4</sup>. The averages are computed between  $z_{\text{inf}}$  and  $z_{\text{sup}}$ , with  $(z_{\text{inf}}, z_{\text{sup}}) = (0, 0.5)$  kpc and  $(z_{\text{inf}}, z_{\text{sup}}) = (0.5, 5)$  kpc for the computation within the disk and the halo, respectively. Figure 12 illustrates the radial profile of metallicity in the disk and in the halo for the three models at three different times. We stress that we consider here only the metallicity contribution of the simulated SF episode, neglecting the initial metal content of the ISM. In this way, we emphasize the role of recent SN feedback in shaping the disk abundance gradient.

The “holes” shown at early times in the radial distribution of the metallicity (e.g. the one present in model MC1 for  $1.4 < R < 2$  kpc, see Figure 12) are due to the absence of recent SN remnants at that radius (cf. the first panel of Figure 9). At later times, when a nearly steady gas circulation is set in (see Section 4.2), the metallicity distribution assumes a smoother profile. We note that the solid line (corresponding to  $t = 30$  Myr) is the lowest one for models MC1 and MC2, but the highest for MC3. In fact, the SNe explode

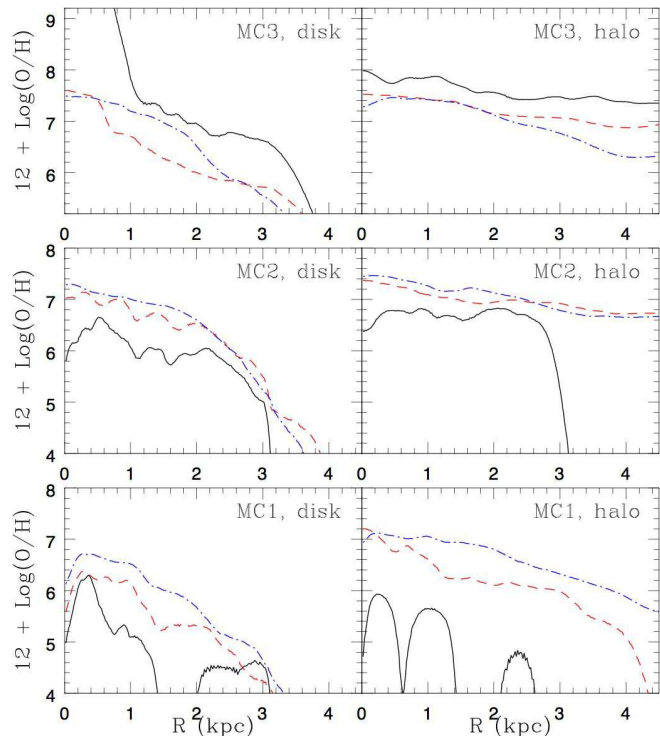


**Figure 12.** Radial distribution of the azimuthal average gas metal abundance in the disk and in the halo of the three models at three different times:  $t = 30$  Myr (solid line),  $t = 100$  Myr (dashed line) and  $t = 250$  Myr (dot-dashed line).

during an extended period in the former two models, gradually increasing the gas metallicity with time. Conversely, in model MC3 all the metals are released very soon, and are then progressively lost by the galaxy; this explains the reduction of the dashed line level ( $t = 100$  Myr). However, at later time the metallicity within the active area of the disk rises again as the metal-rich gas in the halo cools and fall back onto the disk (cf. Figs. 10 and 11). The main result emerging from Figure 12 is that a radial gradient of metallicity within the disk is substantially always present in every model, preserving, at least in part, the gradient of the stellar (and SN) distribution (cf. Figure 2); on the contrary, only shallow gradients are present in the extra-planar gas located in the halo of all the models. Evidently, given its higher sound speed, the hot, low density gas floating above the disk is mixed by turbulence more effectively than the gas in the disk.

The abundances shown in Figure 12 are mass-averaged values within the whole galactic region. Actually, two gas phases coexist within this region: an hot phase with  $T \geq 10^5$  K, and a cold one with  $10^2 < T < 10^5$  K<sup>5</sup>. As we are interested in the possible role of the SN “fountains” in flattening

<sup>3</sup> Dwarf elliptical galaxies, with no or little ISM, have a dominant early burst of star formation, while the gas rich dwarf irregular galaxies lack evidence for such an event. Skillman & Bender (1995) suggest that this is the cause of the different gas content of the two galaxy types, as the SNs explosions associated to the initial SF episode are able to remove the ISM.

<sup>4</sup> Following Iwamoto et al. (1999) we assume a mean value of  $1.8 M_{\odot}$  for the mass of oxygen delivered by a single SN.

<sup>5</sup> The chosen temperature threshold of  $10^5$  K separating the two phases is somewhat arbitrary. However, the results shown here do not depend strongly on such a choice; in fact, as the maximum of the cooling curve occurs around  $T \sim 10^5$  K, the gas with temperatures up to this value cools rather quickly, becoming incorporated in the “cold” phase independently of the exact value of the chosen threshold temperature (c.f. Recchi & Hensler 2013).

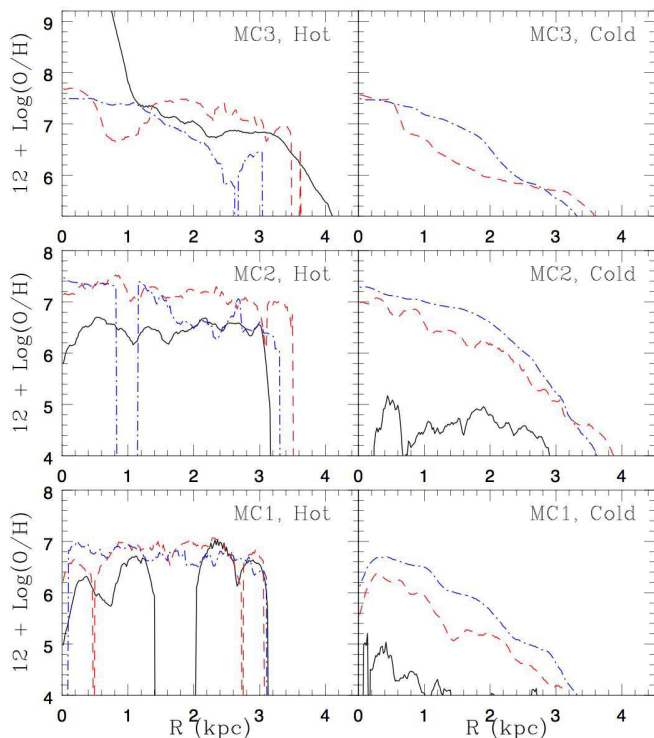


**Figure 13.** Radial distribution of the azimuthal average gas abundance of the metals in the disk of the three models at three different times:  $t = 30$  Myr (solid line),  $t = 100$  Myr (dashed line) and  $t = 250$  Myr (dot-dashed line). Left panels refer to the hot phase ( $T > 10^5$  K), and right panels refer to the cold phase ( $10^2 < T < 10^5$  K).

the radial distribution on the disk of the stellar chemical abundance, we focus now on the cold ISM phase in the disk, out of which new stars will form. Figure 13 illustrates the disk radial profile of the abundance of the cold and hot ISM phases. After a comparison with Figure 12, it turns out that at early times ( $t = 30$  Myr), especially for models MC2 and MC3, the metals reside essentially in the hot phase; this must be expected, as the SN ejecta is found within the hot interiors of superbubbles and chimneys. At later times, however, the ejecta cools down and accumulates into the cold phase which therefore becomes predominant in shaping the total metal distribution. This distribution preserves a substantial gradient, and we thus conclude that the gas circulation due to the SN fountains is ineffective in redistributing the metals and in homogenizing the abundance of the cold ISM and of the next generations of stars. The uniform abundance distribution in the disk of the hot phase established at later times (left panels in Figure 13) would not play any role even if this component would cool at a subsequent stage, because the amount of the hot ejecta at this time is negligible.

As discussed in Appendix A, the numerical diffusion at the contact surfaces separating the hot/cold phase determines an excess of radiative losses. Our tests show that, even under extreme assumptions, the amount of cold gas within the disk does not vary by more than a factor of 2, and its dynamics is not greatly affected. The amount of hot gas and ejecta is instead more sensitive to the cooling prescription

adopted. This, in turn, implies that the radial abundance profiles in the hot phase are affected by radiative cooling, differing by up to a factor of  $\sim 10$  between our standard runs and analogous models without radiative losses. Of course, the latter models are rather extreme and have been calculated only to show the maximum range of variation. However, given the small amount of hot phase ejecta involved (compared to the cold gas), the chemical gradients in the cold disk (which are those influential for the chemical characteristics of the successive generations of stars) persist even in this case, showing that their presence is a robust result of our models.

In Appendix B we tested our results against the numerical resolution. We find that the amount of gas within the disk increases with the grid refinement, but not by a large amount. Our test shows that the disk ISM mass is only  $\lesssim 15\%$  larger when the zone size is decreased by a factor of two. The ejecta mass in the disk is also quite stable: improving the resolution to 10 pc its mass in the disk increases by less than 25%. As a result, the chemical gradients are fairly insensitive on the numerical resolution adopted.

#### 4.5 Flattening of chemical gradients

As no relevant gradient is observed in dwarf galaxies, some mechanisms must be at work in various combinations to distribute metals. Turbulence has been accepted as the major process shaping interstellar medium (cf. the reviews by Elmegreen & Scalo 2004; Scalo & Elmegreen 2004; Burkert 2006, and references therein). However, turbulence has been shown to dissipate quickly if the external driving is stopped, resulting in the need to continuously drive turbulence either locally via stellar feedback or globally via, e.g., clumpy infall of cold gas, spiral density waves, tidal torques, differential rotation, magnetorotational instabilities. SN feedback is likely the most important contributor to ISM turbulence (e.g. Mac Low & Klessen 2004). However, our models indicate that this mechanism is not effective in mixing metals on galactic scales.

Consider, for instance, our model MC1: the SN turbulence do not erase the chemical gradient, originated by the radial distribution of the SNe, which is continuously restored by new explosions (cf. Martin & Roy 1995). However, in case of an intermittent star formation history, other drivers among those listed above could play a role during the inactive phases, as suggested by the flattening of the metallicity gradients in the outer parts of relatively quiescent spiral galaxies (Martin & Roy 1995; Bresolin et al. 2009).

Taking the sound speed  $\sim 10$  km s $^{-1}$  as an upper limit to the velocity at which mixing occurs, it turns out that  $\sim 100$  Myr is a lower limit to the timescale over which chemical gradients are erased over 1 kpc range. Therefore, if the star formation proceeds by bursts separated by quiescent periods of a few hundreds of Myr, as suggested by recent works on H II galaxies (Lagos et al. 2012, and references therein), turbulence may well be the cause of flat chemical gradients.

A further mechanism to flatten chemical gradients has been proposed recently by Schroyen et al. (2011). These authors point out that rotation is a key factor to keep the ISM chemically homogeneous in dwarf galaxies. The resulting “centrifugal barrier”, in fact, prevents the gas from collapsing to the dense central region. This, in turn, results

in a more spatially uniform SFR and, consequently, a flatter stellar mass and abundance profile. This agrees with the observations by Koleva et al. (2009), who found that dwarf galaxies without stellar population gradients are also the fastest rotating ones.

For more continuous star formation regimes, the metal mixing, as discussed above, does not happen fast enough to wipe out the metallicity gradients. A similar conclusion is reached by Werk et al. (2011) about the absence of metallicity gradients in the outskirts of typical star-forming spiral galaxies. In these cases, a clear explanation for the flatness of the chemical distribution is still missing. Given the fast mixing speeds required, the metal transport may be occurring predominantly in a hot gas component, as proposed by Tassis et al. (2008). Our models provide only limited support for this scenario. The abundance gradient in the hot gas in the halo is essentially flat, but to be truly effective this mechanism requires that the majority of the ejecta is in the hot halo phase, where its abundance homogenizes and rains back into the disk. Instead, in our models about half of the SN metals always resides in the cold gas within the disk, exhibiting a negative gradient. Unfortunately, due to numerical diffusion, the amount of the ejecta which remains confined within the disk during the burst is likely overestimated in our models. Higher resolution simulations are needed to evaluate more accurately the amount of metals that can be transported into the hot phase, and then quickly cooled to reproduce the observed flat chemical distribution.

Finally, we point out that, in addition to the physical processes previously outlined, there is a further mechanism usually neglected, but likely relevant in this context. Marcolini et al. (2004) showed that the amount of the SN ejecta retained by the galaxy is quite sensitive to the ram pressure due to the motion of the galaxy through the intra-cluster or intragroup medium. In fact, the ram pressure can push the ejecta “floating” in the halo back toward the disk, increasing the fraction of the metals trapped into the disk by a factor depending on the orientation of the galaxy with respect to the direction of motion. The disk enrichment process is thus also affected by the environment in a complex way, not investigated here.

## 5 SUMMARY AND CONCLUSIONS

As discussed in Section 2.1, we considered a dwarf galaxy with the initial ISM distribution in rotational equilibrium within a gravitational well due to both the stellar disk and the spherical dark matter halo. The aim of the paper was to study the large scale gas flow induced by SN feedback during the “quiescent” (non star-bursting) stage representing the largest phase of the life of dwarf galaxies (Lee et al. 2009), and three regimes of star formation were considered. In particular, we focused on the circulation and distribution of the metals delivered by the SNe, in an attempt to reproduce substantially flat metallicity gradients as those observed.

In agreement with previous theoretical studies (e.g. Mac Low & Ferrara 1999; D’Ercole & Brighenti 1999; Melioli et al. 2013), the absence of substantial ISM loss is verified in our models, even when the SN energy injected is comparable to the ISM binding energy. This is because the

radiative cooling is effective in neutralizing the SN heating and because the flattened distribution of the ISM does not allow an efficient coupling between the SN energy and the gas.

Despite the absence of a sizeable gas removal from the galaxy, the SN feedback has nevertheless a profound impact in the galactic evolution. In fact, even a relatively weak SFR, as the one of model MC2, is able to temporarily lower the ISM density and stop the SF process. At the end of the SN activity, the expelled ISM begins to slowly fall back to the disk, re-building a massive, cold ISM in  $\approx 10^8$  yr, possibly giving rise to a new SF episode, and leading to an intermittent SF history.

For the weakest SFR considered here, model MC1, the SN feedback is instead unable to drastically affect the ISM. In this case the SN associations generate holes in the gaseous disk but do not evacuate completely the active region, and the star formation can continue for long time at a similar rate.

For all the models discussed here the flow triggered by the SN heating generates a long-lived extra-planar gas, especially conspicuous for models MC2 and MC3, as those actually observed in dwarf galaxies.

The circulation of the SN ejecta is rather different from that of the ISM. When the bubbles break out, some or most of their hot interior is expelled with velocities larger than the escape velocity. As a result, after 250 Myr the SN ejecta present in the galaxy (both in the disk and the halo) is anti-correlated to the SN rate, being 100%, 75% and 20% of the total amount for models MC1, MC2 and MC3, respectively. The trapped ejecta is nearly equally accommodated in the disk and in the halo for all the models.

Despite the reduced size and the shallow potential of the dwarf galaxies, the SN ejecta does not spread all over the disk, and does not give rise to the observed nearly flat metal distribution. Instead, the models presented here show the existence of persistent chemical radial gradients as in Milky Way-sized galaxies, where galactic fountains do not lead to efficient radial metal mixing (Melioli et al. 2008, 2009). In Section 4.5 we discussed several mechanisms which could be at work in flattening the chemical gradients, and their compatibility with our models.

## ACKNOWLEDGMENTS

We are grateful to the unknown referee whose suggestions and criticisms substantially improved the paper. CM acknowledges financial support from grants from the Brazilian Agencies FAPESP. FB is supported in part by the Prin MIUR grant 2010LY5N2T “The Chemical and Dynamical Evolution of the Milky Way and Local Group Galaxies”.

## REFERENCES

- Borkowski K. J., Balbus S. A., Fristrom C. C., 1990, ApJ, 355, 501
- Bregman J. N., 1980, ApJ, 236, 577
- Bresolin F., Ryan-Weber E., Kennicutt R. C., Goddard Q., 2009, ApJ, 695, 580
- Brighenti F., Mathews W. G., 1996, ApJ, 470, 747

- Burkert A., 2006, *Comptes Rendus Physique*, 7, 433
- Creasey P., Theuns T., Bower R. G., 2013, *MNRAS*, 429, 1922
- Dalgarno A., McCray R. A., 1972, *Annual Review of Astronomy and Astrophysics*, 10, 375
- Davies J. I., Phillipps S., 1988, *MNRAS*, 233, 553
- de Avillez M. A., 2000, *MNRAS*, 315, 479
- de Avillez M. A., Berry D. L., 2001, *MNRAS*, 328, 708
- de Avillez M. A., Breitschwerdt D., 2004, *A&A*, 425, 899
- , 2005a, *A&A*, 436, 585
- , 2005b, *ApJ*, 634, L65
- De Young D. S., Heckman T. M., 1994, *ApJ*, 431, 598
- Dekel A., Silk J., 1986, *ApJ*, 303, 39
- D’Ercole A., Brighenti F., 1999, *MNRAS*, 309, 941
- Elmegreen B. G., Scalo J., 2004, *ARA&A*, 42, 211
- Fragile P. C., Murray S. D., Lin D. N. C., 2004, *ApJ*, 617, 1077
- Higdon J. C., Lingenfelter R. E., 2005, *ApJ*, 628, 738
- Hill A. S., Joung M. R., Mac Low M.-M., Benjamin R. A., Haffner L. M., Klingenberg C., Waagan K., 2012, *ApJ*, 750, 104
- Hopkins A. M., Schulte-Ladbeck R. E., Drozdovsky I. O., 2002, *AJ*, 124, 862
- Hopkins P. F., Quataert E., Murray N., 2012, *MNRAS*, 421, 3522
- Hunter D. A., Elmegreen B. G., 2004, *AJ*, 128, 2170
- Iwamoto K., Brachwitz F., Nomoto K., Kishimoto N., Umeda H., Hix W. R., Thielemann F.-K., 1999, *ApJS*, 125, 439
- Kennicutt Jr. R. C., 1998, *ApJ*, 498, 541
- Koleva M., de Rijcke S., Prugniel P., Zeilinger W. W., Michielsen D., 2009, *MNRAS*, 396, 2133
- Koo B.-C., McKee C. F., 1992, *ApJ*, 388, 93
- Korpi M. J., Brandenburg A., Shukurov A., Tuominen I., 1999, *A&A*, 350, 230
- Lagos P., Telles E., Muñoz-Tuñón C., Carrasco E. R., Cuisinier F., Tenorio-Tagle G., 2009, *AJ*, 137, 5068
- Lagos P., Telles E., Nigoche Netro A., Carrasco E. R., 2012, *MNRAS*, 427, 740
- Lee J. C., Kennicutt Jr. R. C., Funes S. J. J. G., Sakai S., Akiyama S., 2009, *ApJ*, 692, 1305
- Leitherer C., Schaerer D., Goldader J. D., González Delgado R. M., Robert C., Kune D. F., de Mello D. F., Devost D., Heckman T. M., 1999, *ApJS*, 123, 3
- Lianou S., Cole A. A., 2013, *A&A*, 549, A47
- Loose H.-H., Thuan T. X., 1986, *ApJ*, 309, 59
- Mac Low M.-M., Ferrara A., 1999, *ApJ*, 513, 142
- Mac Low M.-M., Klessen R. S., 2004, *Reviews of Modern Physics*, 76, 125
- Mannucci F., Della Valle M., Panagia N., Cappellaro E., Cresci G., Maiolino R., Petrosian A., Turatto M., 2005, *A&A*, 433, 807
- Marcolini A., Brighenti F., D’Ercole A., 2004, *MNRAS*, 352, 363
- Marcolini A., D’Ercole A., Brighenti F., Recchi S., 2006, *MNRAS*, 371, 643
- Marcolini A., Sollima A., D’Ercole A., Gibson B. K., Ferraro F. R., 2007, *MNRAS*, 382, 443
- Martin P., Roy J.-R., 1995, *ApJ*, 445, 161
- Mayer L., Mastropietro C., Wadsley J., Stadel J., Moore B., 2006, *MNRAS*, 369, 1021
- McQuinn K. B. W., Skillman E. D., Cannon J. M., Dalcanton J., Dolphin A., Hidalgo-Rodríguez S., Holtzman J., Stark D., Weisz D., Williams B., 2010, *ApJ*, 724, 49
- Melioli C., Brighenti F., D’Ercole A., de Gouveia Dal Pino E. M., 2008, *MNRAS*, 388, 573
- , 2009, *MNRAS*, 399, 1089
- Melioli C., de Gouveia Dal Pino E. M., Geraissate F. G., 2013, *MNRAS*, 430, 3235
- Mori M., Ferrara A., Madau P., 2002, *ApJ*, 571, 40
- Navarro J. F., Frenk C. S., White S. D. M., 1996, *ApJ*, 462, 563
- Parkin E. R., Pittard J. M., 2010, *MNRAS*, 406, 2373
- Raga A. C., Navarro-González R., Villagrán-Muniz M., 2000, *RMxAA*, 36, 67
- Recchi S., Hensler G., 2013, *ArXiv e-prints*
- Recchi S., Matteucci F., D’Ercole A., 2001, *MNRAS*, 322, 800
- Recchi S., Matteucci F., D’Ercole A., Tosi M., 2002, *A&A*, 384, 799
- Roychowdhury S., Chengalur J. N., Begum A., Karachentsev I. D., 2009, *MNRAS*, 397, 1435
- Scalo J., Elmegreen B. G., 2004, *ARA&A*, 42, 275
- Schroyen J., de Rijcke S., Valcke S., Cloet-Osselaer A., Dejonghe H., 2011, *MNRAS*, 416, 601
- Shapiro P. R., Field G. B., 1976, *ApJ*, 205, 762
- Shi Y., Helou G., Yan L., Armus L., Wu Y., Papovich C., Stierwalt S., 2011, *ApJ*, 733, 87
- Silk J., Wyse R. F. G., Shields G. A., 1987, *ApJ*, 322, L59
- Skillman E. D., Bender R., 1995, in *Revista Mexicana de Astronomia y Astrofisica*, vol. 27, Vol. 3, Rev. Mex. Astron. Astrofis., Soc. Conf., Pena M., Kurtz S., eds., p. 25
- Strickland D. K., Stevens I. R., 2000, *MNRAS*, 314, 511
- Sutherland R. S., Dopita M. A., 1993, *ApJS*, 88, 253
- Tassis K., Kravtsov A. V., Gnedin N. Y., 2008, *ApJ*, 672, 888
- Tolstoy E., Hill V., Tosi M., 2009, *ARA&A*, 47, 371
- Tomisaka K., Ikeuchi S., 1986, *PASJ*, 38, 697
- van Leer B., 1982, in *Lecture Notes in Physics*, Berlin Springer Verlag, Vol. 170, *Numerical Methods in Fluid Dynamics*, Krause E., ed., pp. 507–512
- van Zee L., Haynes M. P., Salzer J. J., Broeils A. H., 1997, *AJ*, 113, 1618
- Ward-Thompson D., 2002, *Science*, 295, 76
- Weisz D. R., Dalcanton J. J., Williams B. F., Gilbert K. M., Skillman E. D., Seth A. C., Dolphin A. E., McQuinn K. B. W., Gogarten S. M., Holtzman J., Rosema K., Cole A., Karachentsev I. D., Zaritsky D., 2011, *ApJ*, 739, 5
- Weisz D. R., Skillman E. D., Cannon J. M., Dolphin A. E., Kennicutt Jr. R. C., Lee J., Walter F., 2008, *ApJ*, 689, 160
- Werk J. K., Putman M. E., Meurer G. R., Santiago-Figueroa N., 2011, *ApJ*, 735, 71
- Young L. M., van Zee L., Lo K. Y., Dohm-Palmer R. C., Beierle M. E., 2003, *ApJ*, 592, 111
- Zhao Y., Gu Q., Gao Y., 2011, *AJ*, 141, 68

## APPENDIX A: RADIATIVE COOLING EFFECTIVENESS

In Section 4.3 we highlighted the importance of the radiative cooling in regulating the amount of the cold ISM, out of which new generations of stars can form. Unfortunately,



an unavoidable limit of the numerical simulations is given by the inaccurate reproduction of the contact discontinuities separating the hot and cold phases such as those between the hot bubble interiors and the cold shells. In fact, the numerical diffusion tends to smear such discontinuities creating regions of intermediate temperatures and densities; as a consequence, the radiative cooling and the mixing of the hot metals with the surrounding cold ISM are artificially increased<sup>6</sup>.

Underestimates as well as overestimates of the radiative cooling may also occur when a cooling curve calculated in a regime of ionization equilibrium is adopted (as we actually do). A hot plasma may cool at lower rates (Sutherland & Dopita 1993) or at higher rates (e.g. Borkowski et al. 1990) relative to the condition of ionization equilibrium, depending on its thermal history.

In order to ascertain the sensitivity of the results to the radiative effectiveness, we run two additional models of MC3 in which the cooling term is multiplied by the factor  $\eta = 0.17$  and  $\eta = 0$  (adiabatic case), respectively. Figure A1 shows the gas distribution on the  $x = 0$  plane of the two models, as well as of the standard model with  $\eta = 1$ . It is apparent that the models with  $\eta = 1$  and  $\eta = 0.17$  are quite similar. We conclude that, at least for a general description of the gas circulation, the exact shape of the cooling curve is not crucial and the rate of radiative losses is more dependent, on (the square of) the gas density.

A more quantitative evaluation of the effect of the radiative effectiveness is shown in Figure A2. In the two panels the amounts of cold gas ( $T \leq 10^5$  K) in the disk region where the SN explosions occur (that is, in the region defined by  $R < 3$  kpc;  $z < 500$  pc) for models MC2 and MC3 are compared for the cases  $\eta = 1$  and  $\eta = 0$ .

One can see that, in model MC3, the cold gas evolution in the adiabatic case follows the same “trajectory” of the full radiative case, and starts to deviate from it only at  $t \sim 160$  Myr; after 250 Myr the amount of cold gas in the adiabatic model is 40% lower than in the fully radiative case. The model MC2 follows the same qualitative behaviour, but the adiabatic and the radiative models start to differ after  $\sim 90$  Myr; at  $t = 250$  Myr the cold gas in the adiabatic model is nearly half than in the radiative model. This larger discrepancy is due to the fact that in model MC3 the higher SN luminosity heats the gas to higher temperature, which results in a longer (average) cooling time. Moreover, many superbubbles coalesce, reducing the global extension of the contact surface between hot and cold ISM (where most of the radiative losses occurs). In model MC2, where the SN luminosity is lower and prolonged, the heated gas acquires a lower temperature and, consequently, a shorter cooling time. In addition, the weaker SN feedback allows the survival of both cold and hot gas in the active region; this leads to an increase of the contact surfaces. Both effects exacerbate the spurious overcooling.

As a further test we run the model MC3 with  $\eta = 1$  and

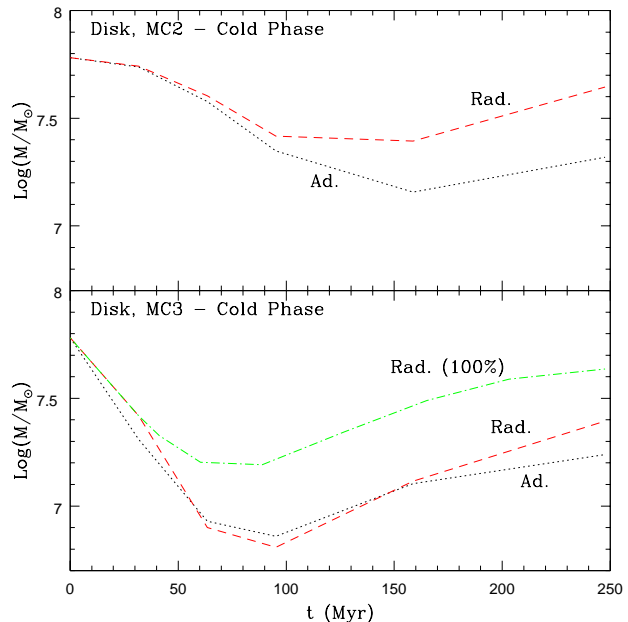


**Figure A2.** Time evolution of the amount of the cold ( $T \leq 10^5$  K) ISM phase within the disk for model MC2 (upper panel) and MC3 (lower panel). The dashed and dotted lines refer to the cases  $\eta = 1$  and  $\eta = 0$ , respectively. The dot-dashed line in the lower panel, labelled as “100%”, represents the mass evolution once our assumption on the dependence of the cooling rate on  $z$  (cf. Section 2.3) is dropped. Masses are given in solar masses.

dropping our assumption on the dependence of the cooling rate on  $z$  (cf. Section 2.3). The result is illustrated by the dot-dashed line in the lower panel of Figure A2. In this case the amount of cold mass is higher relative to the “standard” model by a factor within 1.5 – 2.5, which is an overestimate of the realistic value (due to numerical overcooling).

The above discussion shows that numerical uncertainties in the radiative losses likely do not strongly affect the amount and the dynamics of the cold gas in the disk, unless a prolonged, low intensity SN activity is going on. Sadly, the situation is more complicated for the processes of metal dispersal and mixing. Figure A3 shows the evolution of the mass of the SN ejecta in the hot ( $T > 10^5$  K) phase located in the disk region (and bounded by  $R < 3$  kpc), for the standard models MC2 and MC3 and the corresponding adiabatic analogues. For MC2 the difference in  $M_{\text{ej}}^{\text{hot}}$  is moderate, less than a factor of 2 for most of the time. This relatively small difference is partly due to our choice to artificially reduce the radiative losses near the galactic plane (cfr. Section 2.3). However, the continuous energy injection by SNe, characteristic of this model, also helps to mitigate the overcooling problem described above.

In fact, for model MC3, the difference between the standard and the adiabatic run is more dramatic. At  $t \sim 60$  Myr the discrepancy in  $M_{\text{ej}}^{\text{hot}}$  amounts to about a factor of 10.

This comparison between extreme models (radiative and adiabatic) gives a measure of the uncertainties due to the inaccurate numerical description of the surfaces separating hot and cold gas. While this error seems acceptable for models MC1 (not shown here) and MC2, we are not in

<sup>6</sup> Actually, a physical spread of the contact discontinuities is expected owing to the presence of thermal conduction and mixing layers, but, in general, it remains too thin to be properly resolved by large scale numerical simulations (c.f. Recchi et al. 2001; Marcolini et al. 2004; Parkin & Pittard 2010)

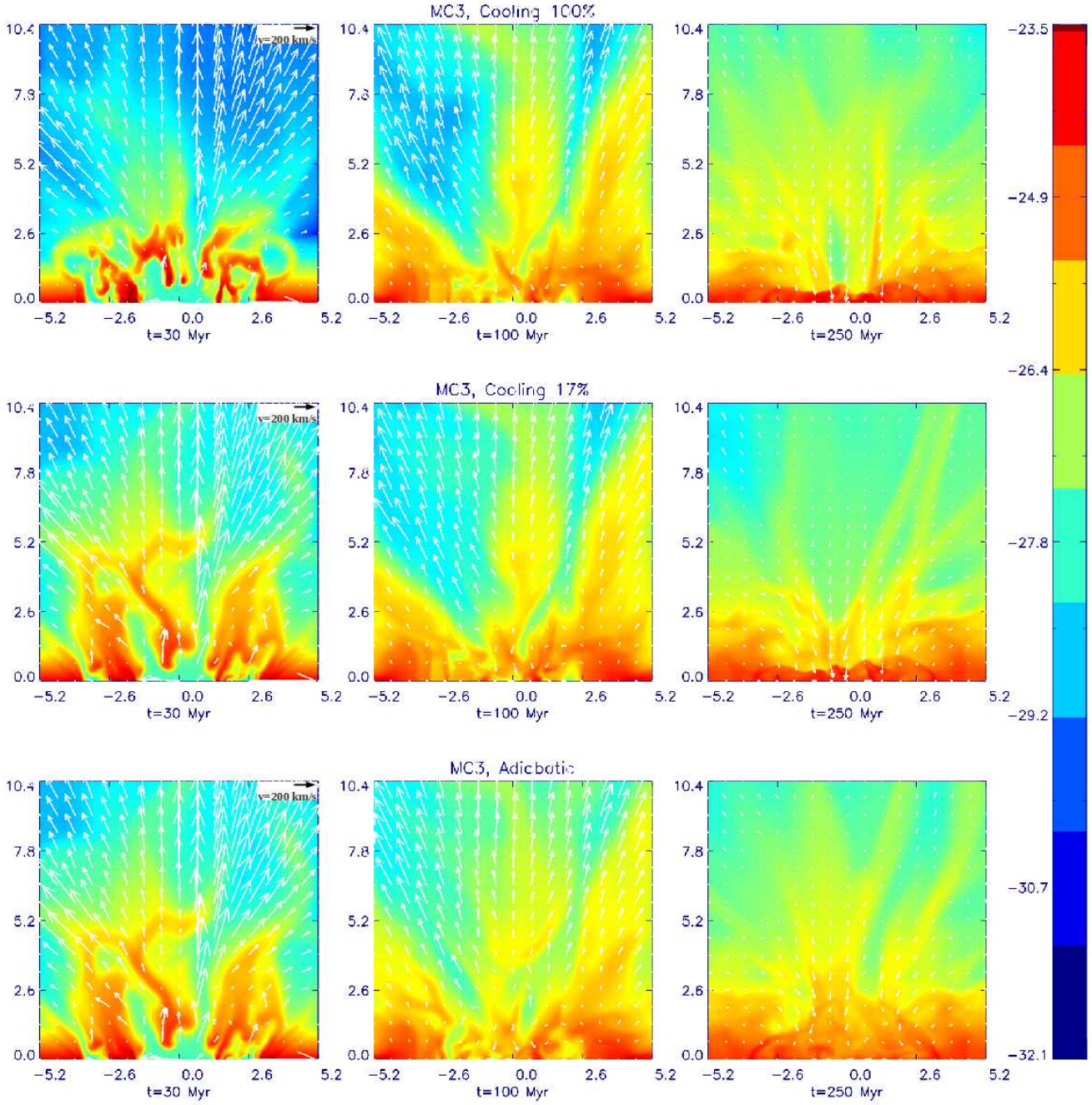


**Figure A1.** Gas density distribution on the  $x = 0$  plane for model MC3. From top to bottom, the rows refer to a radiative cooling efficiency  $\eta = 1$ ,  $\eta = 0.17$  and  $\eta = 0$ , respectively. Each column refers to a single time. The dashed circle delimitates the active area (see text). Distances are in kpc and the (horizontal)  $x$ -axis and (vertical)  $z$ -axis individuate the plane perpendicular to the galactic disk at  $R=0$ . Densities are in  $\log(\text{g cm}^{-3})$  units.

the position to make strong statement for model MC3, for  $t \geq 60$  Myr. Higher resolution simulations (in preparation) will shed light on this issue.

## APPENDIX B: CONVERGENCE TEST

Here we describe how the grid resolution influence our results, in particular the amount of gas mass in the disk which impacts on the possible formation of chemical gradients.

To this aim, we run a test model with three different maximum resolutions:  $\Delta x = 40, 20, 10$  pc. In order to save computational time, the test model is a modified version of model MC3. Here the computational grid covers the region

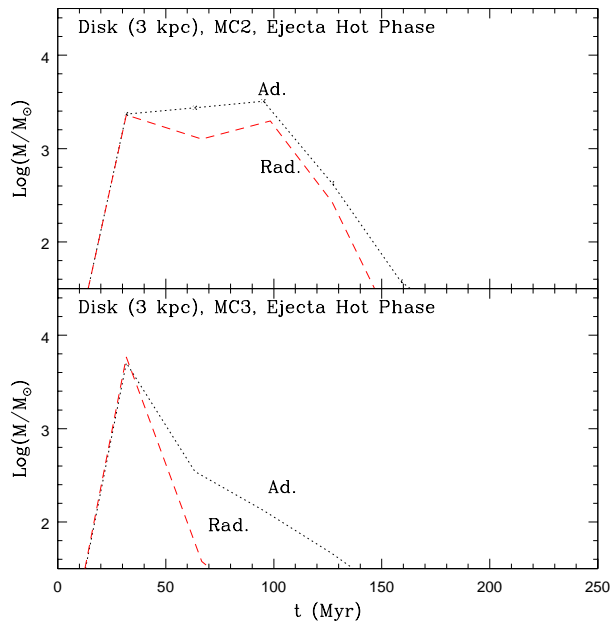


**Figure A3.** Time evolution of the amount of the hot ( $T > 10^5$  K) ejecta phase within the active area of the disk ( $R \leq 3$  kpc) for model MC2 (upper panel) and MC3 (lower panel). The dashed and dotted lines refer to the cases  $\eta = 1$  and  $\eta = 0$ , respectively. Masses are given in solar masses.

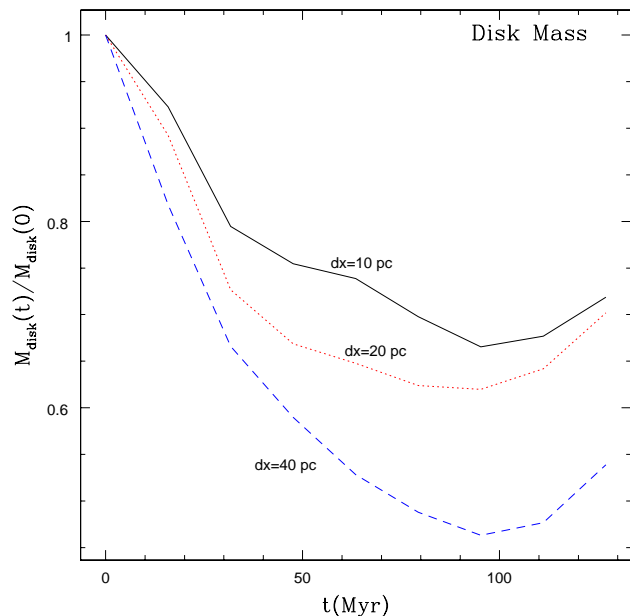


**Figure B1.** Time evolution of disk gas mass for different grid resolution for our test model.

$-2.5 < x < 2.5$  kpc,  $-2.5 < y < 2.5$  kpc,  $z < 5$  kpc, while the active region is limited to  $R = 1.5$  kpc. The results for the ISM mass in the disk (one of the most sensitive quantity) are illustrated in Figure B1, where it can be seen that  $M_{\text{disk}}(t)$  weakly increases with the resolution. The reason for this trend is twofold: *i*) the higher resolution generates smaller structures in the contact discontinuities, increasing their total surface. As significant radiative losses occur on these surfaces, less SN energy is available to lift the ISM; *ii*) a higher resolution reduces the numerical viscosity, diminishing the ability of the hot wind to drag the cold ISM. As the models presented in the text are computed with  $\Delta x = 20$  pc resolution, the values of the mass content found in the galactic disk represent lower limits.

We examined also the behaviour of the ejecta mass in the disk. We find that increasing the resolution to 10 pc its value increases by less than 25%, in line with the disk ISM trend. With a coarser grid with zone size of 40 pc, however, results start to diverge more, with the disk ejecta mass lowered by a factor of  $\sim 4$ . We conclude that the resolution adopted for our models (20 pc) is high enough to give meaningful results.

